THE EUROPEAN
PHYSICAL JOURNAL C

Holographic model for light quarks in anisotropic hot dense QGP with external magnetic field

Irina Ya. Aref'eva[a], Alexey Ermakov[b], Kristina Rannu[c] , Pavel Slepov[d]

Steklov Mathematical Institute, Russian Academy of Sciences, Gubkina str. 8, Moscow 119991, Russia

Abstract We present a five-dimensional twice anisotropic holographic model supported by Einstein-dilaton-three-Maxwell action describing light quarks. The first of the Maxwell fields provides finite chemical potential. The second Maxwell field serves for anisotropy, characterizing spatial anisotropy of the QGP produced in heavy-ion collisions (HIC). The third Maxwell field is related to a magnetic field that appears in HIC. The dependence of the 5-dim black hole solution and confinement/deconfinement phase diagram on this magnetic field is considered. The effect of the inverse magnetic catalyses for light quarks phase diagram is obtained. Positions of critical end points are found. We also study the behavior of the conductivity for light quarks in both isotropic and anisotropic cases and show that behaviour of the conductivity near critical points essentially depend on quark masses, meanwhile at high temperature they are similar.

Contents

1 Introduction

Holographic duality provides an effective approach to study nonperturbative properties of QCD [1–3]. One of the achievements of the QCD holographic description is that holographic QCD (HQCD) models can describe QCD at all energy scales [4,5]. HQCD reproduces properties of QCD obtained by others methods, namely perturbative renormalization group and lattice approach. However neither of these methods can describe QCD with non-zero chemical potential and therefore predict the phase diagram for quark-gluon plasma (QGP). Nowadays this goal is achieved by holographic methods only. There are HQCD models that describe QCD with heavy quarks [6], light quarks [7] as well as with realistic quarks contents [8]. These models are based on the so-called "bottom-up" holographic approach. Holographic method can also describe anisotropic dense matter in external magnetic field.

The goal of this paper is to study the behaviour of anisotropic QCD with light quarks in strong external magnetic field. This paper is the generalization of our consideration of anisotropic QCD with heavy quarks in external magnetic field [9,10] on the one hand and of our consideration of anisotropic QCD with light quarks at zero magnetic field [11] to the case of non-zero external field on the other hand.

The model under consideration [12] has been built using a potential reconstruction method [1–7,9–11,13–32]. This model is characterized by a five-dimensional Einstein-dilaton-Maxwell action and a five-dimensional metric with

[a] e-mail: arefeva@mi-ras.ru

[b] e-mail: ermakov.av15@physics.msu.ru

[c] e-mail: rannu-ka@rudn.ru (corresponding author)

[d] e-mail: slepov@mi-ras.ru

a warp factor that tunes the blackening function and, consequently, the thermodynamics of the model. The phase transition structure of HQCD strongly depends on the warp factor choice. The simplest warp factor has an exponential form with a quadratic polynomial [6,33]. It reproduces the first-order phase transition from lattice calculations (Columbia plots [34,35]) for the heavy quarks. To reproduce the first-order phase transition for the light quarks one has to use rational functions [5,7].

To describe the QGP produced in heavy ion collisions (HIC) by holographic methods one has to make more modifications of the five-dimensional metric. These modifications are related to two types of the anisotropy that take place in HIC: (i) anisotropy between the longitudinal and transversal directions and (ii) anisotropy in the transversal plane related to magnetic field produced in non-central collisions of ions. It was proposed to characterize the first type of anisotropy by a parameter ν that is similar to the Lifshitz parameter of the AdS metric modification. The isotropic model corresponds to $\nu = 1$. For the value of about $\nu = 4.5$ the energy dependence of the entropy produced in the HIC agrees with the experimental data [36] for the energy dependence of the total multiplicity of created particles [37]. The magnetic field created by non-central ion collisions [38] produces anisotropy in the plane transverse to the ion collision axis. Therefore, it is important to consider these types of anisotropy in holographic models [9,10,24,39–47]. To construct anisotropic models, one considers an additional Maxwell field to support the anisotropy in metrics [9–11,13,15,16,19–21,23,24,26,32,37,48]. Note that calculations in the twice anisotropic model for the light quarks are much more complicated than for the heavy quarks [9,24], since the warp factor and the kinetic gauge function f_1 have more complex form. For the heavy quark model we have found [9,10] the effect of the inverse magnetic catalysis (IMC) – larger absolute values of the coupling coefficient c_B lead to decrease of the transition temperature. In the model for the light quarks considered in this paper we also find the IMC. This work is a generalization of results obtained in [9,11] to the case of twice anisotropic holographic light quark model. The results obtained in [11] are generalized to the case of present of an external magnetic field, and the results obtained in [9,10] to the case of light quarks.

We also study electrical transport properties of QGP and its relation to the thermal direct photon production in the line of previous studies of these problems for other holographic models [49–56]. Photons do not interact with QGP hadronic matter and therefore provide information about various characteristics of QGP including phase structure at different time scales. It is well known that the direct photons (DP) emission rate is connected to the conductivity of QGP [57,58]. In this work we generalize results of [32] concerning the conductivity and photon production to the light quarks case. We show that conductivity both in longitudinal and transverse directions essentially depends on anisotropy parameter ν. The DP flow also depends on temperature and other thermodynamic properties of QGP. Like it was in the heavy quarks case, for the light quarks the higher the magnetic field or/and chemical potential, the higher the conductivity. We will see that for $\nu = 1$ the conductivity behavior for the heavy and light quarks is different at near-critical temperatures, but at high temperatures they both saturate to constant values. For $\nu = 4.5$ the conductivity behavior for the heavy and light quarks is also different at near-critical temperatures as well as at high temperatures. Conductivity for the light quarks model along the collision direction monotonically decreases with temperature while transversal components have minimum and increase at large temperatures. Since we expect isotropisation [19,59,60], i.e. $\nu \to 1$ in about $1 - 5fm/c \sim 10^{-24}s$, we expect essential change of conductivity at this time scale.

The paper is organized as follows. In Sect. 2 the holographic model is presented. In Sect. 3 the thermodynamics of the model and behaviour of the Wilson loops are described, the confinement/deconfinement phase diagram is obtained. Sect. 4 describes the derivation of the direct photons and electrical conductivity properties. In Sect. 5 we summarize our results and discuss future directions of investigations.

2 Model

In this section we present a model suitable for the light quarks' version of the confinement/deconfinement phase diagram [11] in magnetic field similar to how it was done in our work [9,10].

2.1 Metric and EOM

Here we take the same action as in our previous work [9]. In Einstein frame it has the following form

$$S = \int \frac{d^5x \sqrt{-g}}{16\pi G_5} \left[R - \frac{f_1(\phi)}{4} F_{(1)}^2 - \frac{f_2(\phi)}{4} F_{(2)}^2 \right.$$
$$\left. - \frac{f_B(\phi)}{4} F_{(B)}^2 - \frac{\partial_\mu \phi \partial^\mu \phi}{2} - V(\phi) \right], \qquad (2.1)$$

that is the extended version of the action used in [11,15] and contain an additional term related with external magnetic field $F_{(B)}$. Maxwell field $F_{(1)}$ provides chemical potential μ (see Eq. (2.17) below) and Maxwell field $F_{(2)}$ provides primary anisotropy ν (associated with longitudinal/transversal anisotropy).

We use the same metric anzatz as in [9]:

$$ds^2 = \frac{L^2\, \mathfrak{b}(z)}{z^2}\left[-g(z)dt^2 + dx^2 + \left(\frac{z}{L}\right)^{2-\frac{2}{\nu}} dy_1^2 \right.$$

$$\left. + e^{c_B z^2}\left(\frac{z}{L}\right)^{2-\frac{2}{\nu}} dy_2^2 + \frac{dz^2}{g(z)} \right], \tag{2.2}$$

$$\mathfrak{b}(z) = e^{2\mathcal{A}(z)}. \tag{2.3}$$

The 5-th coordinate z plays the role of the energy scale, the behavior of the scalar field ϕ allows one to control the renormalization group properties. A scalar (dilaton) field's dynamics $\phi = \phi(z)$ describe the running coupling in 4-dim quantum theory, and the 5-th coordinate playes a role of an energy scale. $V(\phi)$ is the scalar field potential.

The difference between "heavy quarks" and "light quarks" cases lies in the form of the warp factor $\mathfrak{b}(z)$. For the heavy quarks we used $\mathfrak{b}(z) = e^{-\frac{cz^2}{2}}$ [15]. To get the "light quarks" version we follow [7] and assume $\mathcal{A}(z) = -a\ln(bz^2 + 1)$. This warp factor reproduces the β-function in isotropic version ($\nu = 1, c_B = 0$).

Here we use the anzats, where the non-zero components of the electro-magnetic field and the field strengths are

$$A_\mu^{(1)} = A_t(z)\delta_\mu^0, \quad F_{y_1 y_2}^{(2)} = q, \quad F_{xy_1}^{(B)} = q_B. \tag{2.4}$$

In action (2.1) $f_1(\phi)$, $f_2(\phi)$ and $f_B(\phi)$ are the coupling functions associated with the Maxwell fields A_μ, $F_{\mu\nu}^{(2)}$ and $F_{\mu\nu}^{(B)}$ correspondingly, q and q_B are constants.

Here parameters ν and c_B have the same meaning as in [9]. The primary anisotropy parameter ν describes non-equivalence between longitudinal and transversal directions. The isotropic case corresponds to $\nu = 1$, while $\nu = 4.5$ reproduces the multiplicity of the charged particles production [37].

We refer to c_B as to the magnetic field parameter that describes non-centrality of the heavy ion collisions. Although explicit relation of c_B to the magnitude of magnetic field is not established, there are considerations suggesting that $B^2 = -c_B$ [45,61]. So we have $c_B < 0$ in all our calculations. Magnetic field parameter c_B is an implicit function of the magnetic charge q_B from the anzats (2.4). However, we will not need the explicit form of this relation in what follows. We usually set $q = q_B = 1$ in numerical calculations. The metric anzats (2.2) also contains the blackening function $g(z)$ which will be determined in the subsequent paragraphs.

Applying the stationary action principle, we get the same equations of motion (EOM) as in [9]:

$$\phi'' + \phi'\left(\frac{g'}{g} + \frac{3\mathfrak{b}'}{2\mathfrak{b}} - \frac{\nu+2}{\nu z} + c_B z\right)$$

$$+ \left(\frac{z}{L}\right)^2 \frac{\partial f_1}{\partial\phi}\frac{(A_t')^2}{2\mathfrak{b}g} - \tag{2.5}$$

$$- \left(\frac{L}{z}\right)^{2-\frac{4}{\nu}} \frac{\partial f_2}{\partial\phi}\frac{q^2\, e^{-c_B z^2}}{2\mathfrak{b}g}$$

$$- \left(\frac{z}{L}\right)^{\frac{2}{\nu}} \frac{\partial f_B}{\partial\phi}\frac{q_B^2}{2\mathfrak{b}g} - \left(\frac{L}{z}\right)^2 \frac{\mathfrak{b}}{g}\frac{\partial V}{\partial\phi} = 0,$$

$$A_t'' + A_t'\left(\frac{\mathfrak{b}'}{2\mathfrak{b}} + \frac{f_1'}{f_1} + \frac{\nu-2}{\nu z} + c_B z\right) = 0, \tag{2.6}$$

$$g'' + g'\left(\frac{3\mathfrak{b}'}{2\mathfrak{b}} - \frac{\nu+2}{\nu z} + c_B z\right) - \left(\frac{z}{L}\right)^2 \frac{f_1(A_t')^2}{\mathfrak{b}}$$

$$- \left(\frac{z}{L}\right)^{\frac{2}{\nu}} \frac{q_B^2\, f_B}{\mathfrak{b}} = 0, \tag{2.7}$$

$$\mathfrak{b}'' - \frac{3(\mathfrak{b}')^2}{2\mathfrak{b}} + \frac{2\mathfrak{b}'}{z} - \frac{4\mathfrak{b}}{3\nu z^2}\left(\frac{\nu-1}{\nu}\right.$$

$$\left. + \left(1 - \frac{3\nu}{2}\right)c_B z^2 - \frac{\nu c_B^2 z^4}{2}\right) + \frac{\mathfrak{b}\,(\phi')^2}{3} = 0, \tag{2.8}$$

$$2g'\frac{\nu-1}{\nu} + 3g\frac{\nu-1}{\nu}\left(\frac{\mathfrak{b}'}{\mathfrak{b}} - \frac{4(\nu+1)}{3\nu z} + \frac{2c_B z}{3}\right)$$

$$+ \left(\frac{L}{z}\right)^{1-\frac{4}{\nu}} \frac{L\,q^2\, e^{-c_B z^2}\, f_2}{\mathfrak{b}} = 0, \tag{2.9}$$

$$2g'\left(1 - \frac{1}{\nu} + c_B z^2\right) + 3g\left[\left(1 - \frac{1}{\nu} + c_B z^2\right)\right.$$

$$\times \left(\frac{\mathfrak{b}'}{\mathfrak{b}} - \frac{4}{3\nu z} + \frac{2c_B z}{3}\right) - \frac{4(\nu-1)}{3\nu z}\bigg] +$$

$$+ \left(\frac{L}{z}\right)^{1-\frac{4}{\nu}} \frac{L\,q^2\, e^{-c_B z^2}\, f_2}{\mathfrak{b}} - \left(\frac{z}{L}\right)^{1+\frac{2}{\nu}} \frac{L\,q_B^2\, f_B}{\mathfrak{b}} = 0, \tag{2.10}$$

$$\frac{\mathfrak{b}''}{\mathfrak{b}} + \frac{(\mathfrak{b}')^2}{2\mathfrak{b}^2} + \frac{3\mathfrak{b}'}{\mathfrak{b}}\left(\frac{g'}{2g} - \frac{\nu+1}{\nu z} + \frac{2c_B z}{3}\right)$$

$$- \frac{g'}{3zg}\left(5 + \frac{4}{\nu} - 3c_B z^2\right)$$

$$+ \frac{8}{3z^2}\left(1 + \frac{3}{2\nu} + \frac{1}{2\nu^2}\right) - \frac{4c_B}{3}\left(1 + \frac{3}{2\nu} - \frac{c_B z^2}{2}\right)$$

$$+ \frac{g''}{3g} + \frac{2}{3}\left(\frac{L}{z}\right)^2 \frac{\mathfrak{b}V}{g} = 0. \tag{2.11}$$

Turning off the external magnetic field, i.e. putting $c_B = q_B = f_B = 0$ into (2.6)–(2.11), we get the EOM from [11]. Normalizing to the AdS-radius, $L = 1$, we get the EOM from

[15]. Excluding anisotropy, i.e. putting $\nu = 1$ and $f_2 = 0$, we get the expressions that fully coincide with the EOM from [6,7]. Thus (2.6)–(2.11) are universal anisotropic EOM, appropriate both for heavy and light quarks description, that include solution from [6,7] as an isotropic limit. We also consider the general form of the boundary conditions:

$$A_t(0) = \mu, \quad A_t(z_h) = 0, \tag{2.12}$$

$$g(0) = 1, \quad g(z_h) = 0, \tag{2.13}$$

$$\phi(z_0) = 0, \tag{2.14}$$

where $z_0 = 0$ corresponds to [7] and $z_0 = z_h$ to [15]. The choice of the boundary condition for the scalar field was discussed in details in [11].

2.2 Solution

Just as it was in previous cases, to solve EOM (2.6)–(2.11) we need to determine the form of the coupling function f_1. Let us take the same form as for the light quarks model [11]. Taking into account the "light quarks" warp factor, we get

$$f_1 = e^{-cz^2 - \mathcal{A}(z)} z^{-2+\frac{2}{\nu}} = (1 + bz^2)^a e^{-cz^2} z^{-2+\frac{2}{\nu}}. \tag{2.15}$$

Solving (2.6) with the coupling function (2.15) and boundary conditions (2.12) gives

$$
\begin{aligned}
A_t &= \mu \frac{e^{(2c-c_B)z^2/2} - e^{(2c-c_B)z_h^2/2}}{1 - e^{(2c-c_B)z_h^2/2}} \\
&\xrightarrow[c_B \to 0]{} \mu \frac{e^{cz^2} - e^{cz_h^2}}{1 - e^{cz_h^2}},
\end{aligned}
\tag{2.16}
$$

$$A_t(z) = \mu - \rho z^2 + \ldots \implies \rho$$
$$= -\frac{\mu(2c - c_B)}{2\left(1 - e^{(2c-c_B)z_h^2/2}\right)}. \tag{2.17}$$

We take $a = 4.046$, $b = 0.01613$, $c = 0.227$ to make our solution agree with the results from [7] in the isotropic case, the results from [11] in the anisotropic case and the results from [9] for the heavy quarks version (Fig. 1). These values are due to the mass spectrum of ρ meson with its excitations and lattice results for the phase transition temperature [7].

To obtain the blackening function we need to know the kinetic function f_B describing coupling to the third Maxwell field $F_{\mu\nu}^{(B)}$. Equation (2.6) is a consequence of the remaining Eqs. (2.6)–(2.11), which is checked directly. Subtracting (2.9) from (2.10), we get an expression for the function f_B

$$f_B = 2\left(\frac{z}{L}\right)^{-2/\nu} \mathfrak{b} g \frac{c_B z}{q_B^2}\left(\frac{3\mathfrak{b}'}{2\mathfrak{b}} - \frac{2}{\nu z} + c_B z + \frac{g'}{g}\right), \tag{2.18}$$

that allows to transform (2.7) into

$$
\begin{aligned}
& g'' + g'\left(\frac{3\mathfrak{b}'}{2\mathfrak{b}} - \frac{\nu + 2}{\nu z} - c_B z\right) \\
& -2g\left(\frac{3\mathfrak{b}'}{2\mathfrak{b}} - \frac{2}{\nu z} + c_B z\right)c_B z - \left(\frac{z}{L}\right)^2 \frac{f_1(A_t')^2}{\mathfrak{b}} = 0
\end{aligned}
\tag{2.19}
$$

and get the solution

$$
\begin{aligned}
g = e^{c_B z^2}&\left[1 - \frac{I_1(z)}{I_1(z_h)} + \frac{\mu^2(2c - c_B)}{L^2\left(1 - e^{(2c-c_B)z_h^2/2}\right)^2}\right. \\
&\times\left[\left\{\left(e^{(2c-c_B)z^2/2} - e^{(2c-c_B)z_h^2/2}\right)I_1(z) - (2c - c_B)I_2(z)\right.\right. \\
&\left.\left.\left.\times\left(1 - \frac{I_1(z)}{I_1(z_h)}\frac{I_2(z_h)}{I_2(z)}\right)\right\}\right]\right],
\end{aligned}
\tag{2.20}
$$

$$I_1(z) = \int_0^z \left(1 + b\xi^2\right)^{3a} e^{-3c_B\xi^2/2} \xi^{1+\frac{2}{\nu}} d\xi, $$

$$
\begin{aligned}
I_2(z) = &\int_0^z e^{(2c-c_B)\xi^2/2} \\
&\times \int_0^\xi \left(1 + b\chi^2\right)^{3a} e^{-3c_B\chi^2/2} \chi^{1+\frac{2}{\nu}} d\chi\, d\xi.
\end{aligned}
\tag{2.21}
$$

However this solution can't be accepted as the final one and should be improved. First of all it can't be shown that our previous "light quarks" blackening function [11] serves as zero magnetic field limit for (2.21). To overcome this difficulty we simplify the expression via partial integration:

$$
\begin{aligned}
g = e^{c_B z^2}&\left[1 - \frac{I_1(z)}{I_1(z_h)} + \frac{\mu^2(2c - c_B)I_2(z)}{L^2\left(1 - e^{(2c-c_B)z_h^2/2}\right)^2}\right. \\
&\left.\times\left(1 - \frac{I_1(z)}{I_1(z_h)}\frac{I_2(z_h)}{I_2(z)}\right)\right],
\end{aligned}
\tag{2.22}
$$

where $I_1(z)$ is described by the corresponding expression from (2.21), but $I_2(z)$ was redefined as

$$I_2(z) = \int_0^z \left(1 + b\xi^2\right)^{3a} e^{(c-2c_B)\xi^2} \xi^{1+\frac{2}{\nu}} d\xi. \tag{2.23}$$

Figure 2 shows the influence of the magnetic field metric backreaction parameter c_B (Fig. 2a, c), chemical potential μ (Fig. 2b, c) and primary anisotopy ν on the blackening function. Positive c_B leads to the local maximum before horizon, while negative c_B decreases the blackening function values till the horizon (Fig. 2a). These effects of the magnetic field are weaker for larger primary anisotropy.

Further solving (2.6)–(2.11) system with the coupling functions (2.15) and (2.18) and the boundary condition (2.14) gives
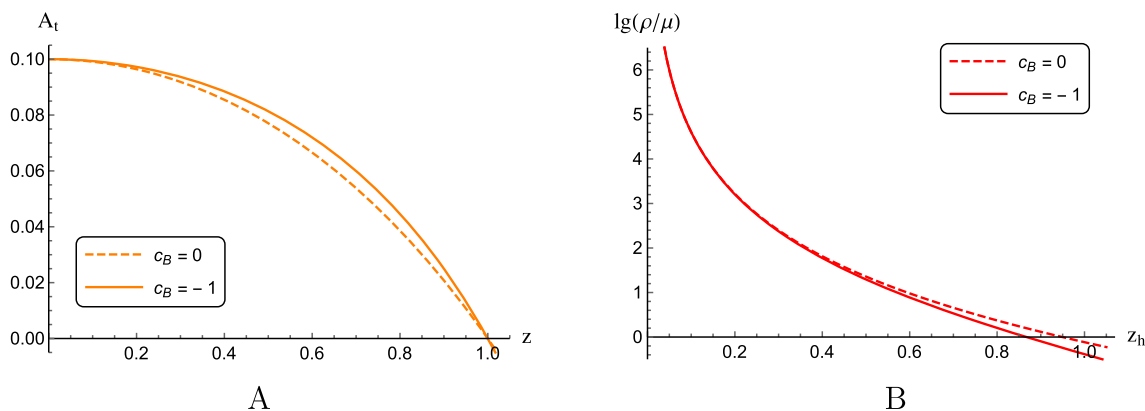
Fig. 1 Electric potential $A_t(z)$ (**a**) and density $\rho(z_h)/\mu$ (**b**) in logarithmic scale for the "light quarks" with (solid lines) and without (dashed lines) magnetic field, $c_B = 0, -1$; $\mu = 0.1$, $a = 4.046$, $b = 0.01613$, $c = 0.227$

$$f_2 = 2\left(\frac{z}{L}\right)^{2-4/\nu} \frac{\nu - 1}{q^2\nu^2z^2} \frac{e^{c_B z^2}}{(1+bz^2)^{2a}}$$

$$\times \left\{\left(2 + 2\nu - \nu c_B z^2 + \frac{6abv z^2}{1+bz^2}\right)g - g'\nu z\right\}, \tag{2.24}$$

$$\phi = \int_{z_0}^{z} \sqrt{\frac{4(\nu-1)}{\nu^2\xi^2} - 2c_B\left(3 - \frac{2}{\nu}\right) - 2c_B^2\xi^2 + \frac{12ab}{1+b\xi^2}\left(1 + 2\frac{1+ab\xi^2}{1+b\xi^2}\right)}\, d\xi, \tag{2.25}$$

$$\phi' = \sqrt{\frac{4(\nu-1)}{\nu^2z^2} - 2c_B\left(3 - \frac{2}{\nu}\right) - 2c_B^2z^2 + \frac{12ab}{1+bz^2}\left(1 + 2\frac{1+abz^2}{1+bz^2}\right)}, \tag{2.26}$$

$$V(z) = -\frac{(1+bz^2)^{2a}\, z}{2L^2}$$

$$\times \left[2\left\{2\frac{(1+\nu)(1+2\nu) + \left(2 + (2+3a)(3+2\nu)\nu\right)bz^2 + (1+\nu+3a\nu)(1+2\nu+6a\nu)b^2z^4}{(1+bz^2)^2\nu^2z^2}\right.\right.$$

$$\left.- c_B\left(2 + \frac{3}{\nu} + \frac{12abz^2}{1+bz^2}\right) + c_B^2z^2\right\}$$

$$\times gz - \left(5 + 3\left(\frac{6ab}{1+bz^2} - c_B\right)z^2 + \frac{4}{\nu}\right)g' + g''z\right]. \tag{2.27}$$

Primary anisotropy leads to divergences of $\phi = \phi(z)$ near $z = 0$ (Fig. 3), reaching a linear dependence afterwards. Further increase of ν doesn't notably change dilaton dependence on z and c_B. Thus it only matters if $\nu = 1$ or $\nu \neq 1$.

Note, that we do not fix coupling function for the 3-rd Maxwell f_B, but derive it from the EOM with intent. Fixing, for example, $f_B = f_1$ makes system (2.6)–(2.11) not selfconsistent, therefore proper solution with the $f_B = f_1$ condition can't be found.

3 Thermodynamics

3.1 Temperature and entropy

For the metric (2.2) and the light quarks warp factor temperature and entropy can be written as:

$$T = \frac{|g'|}{4\pi}\bigg|_{z=z_h}, \quad s = \left(\frac{L}{z_h}\right)^{1+\frac{2}{\nu}} \frac{e^{c_B z_h^2/2}}{4(1+bz_h^2)^{3a}}. \tag{3.1}$$
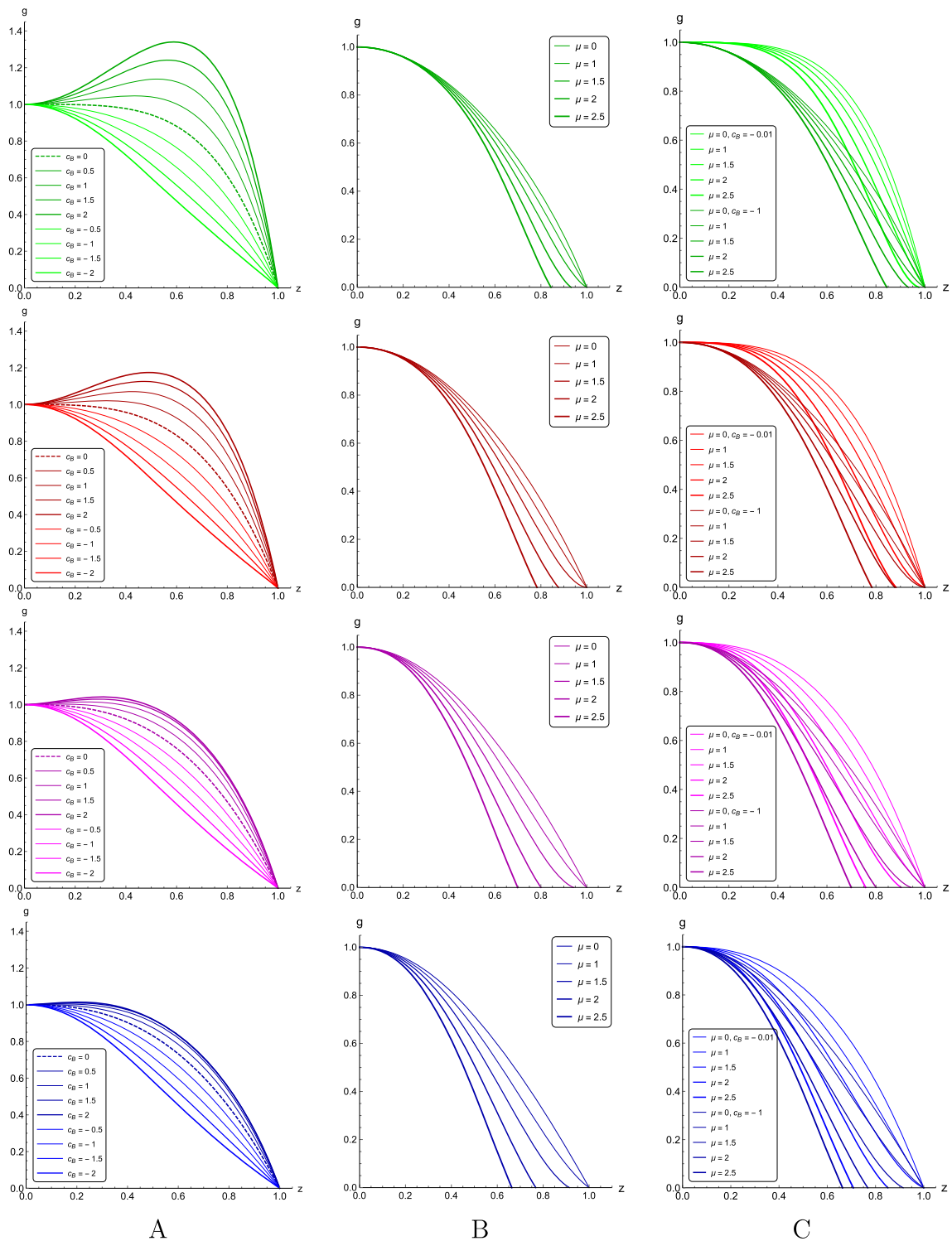
Fig. 2 Blackening function $g(z)$ for different c_B, $\mu = 0$ (**a**), for different μ, $c_B = -1$ (**b**) and for different μ, $c_B = -0.01$ (light curves) and $c_B = -1$ (dark curves) (**c**); $\nu = 1$ (1-st line), $\nu = 1.5$ (2-nd line), $\nu = 3$ (3-rd line) and $\nu = 4.5$ (4-th line), $a = 4.046$, $b = 0.01613$, $c = 0.227$, $z_h = 1$
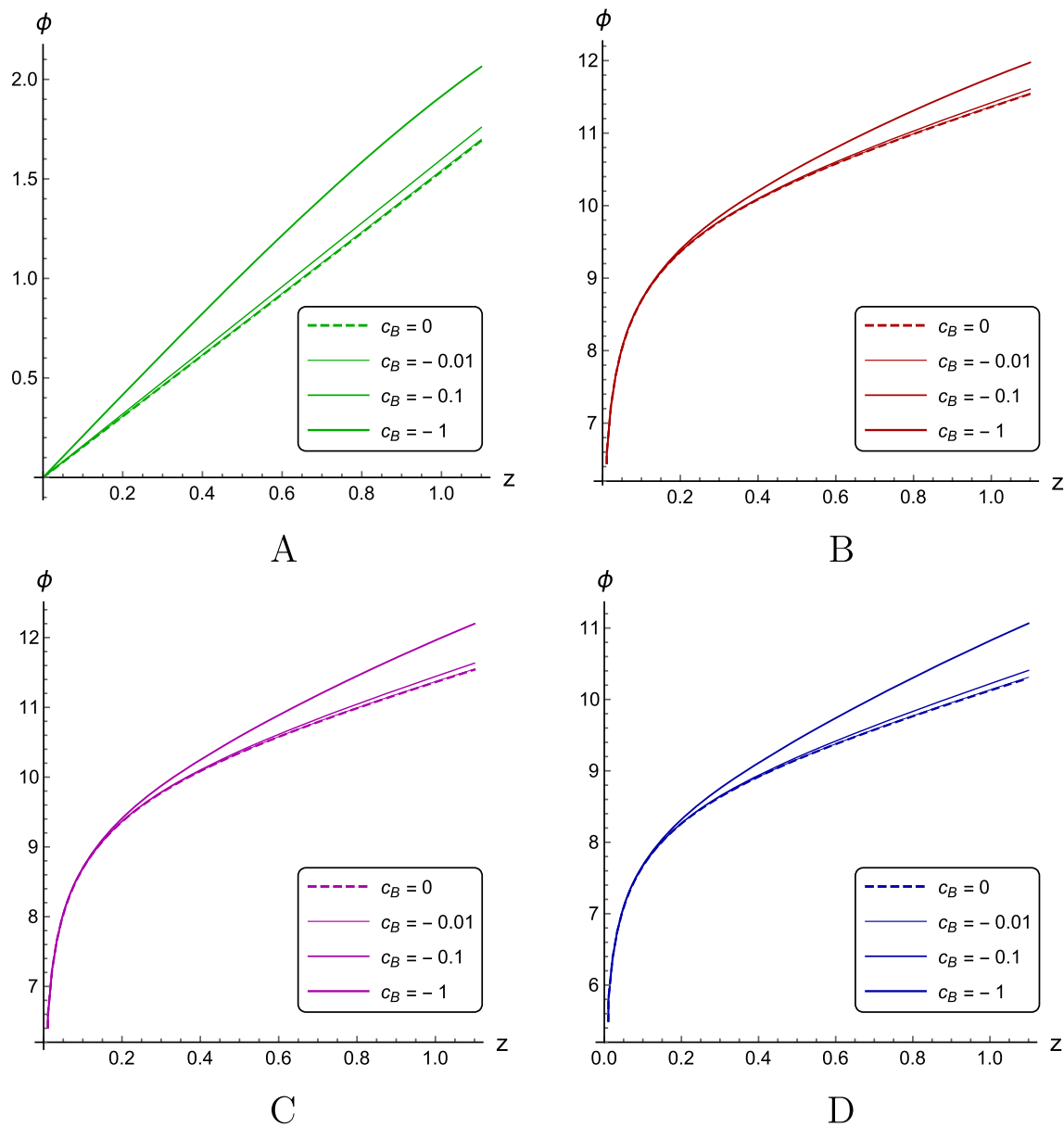
Fig. 3 Scalar field $\phi(z)$ for different c_B for $\nu = 1$ (**a**), $\nu = 1.5$ (**b**), $\nu = 3$ (**c**), $\nu = 4.5$ (**d**), $a = 4.046$, $b = 0.01613$, $c = 0.227$

On Fig. 4 temperature as a function of horizon is presented. The multivalued behavior of $z_h(T)$ preserves starting from the chemical potential value of the so called critical end point (CEP) till another specific chemical potential value for which second horizon appears. For $\nu = 1$ $\mu_{CEP} > 0$, while in cases of primary anisotropy ($\nu = 1.5, 3, 4.5$) $\mu_{CEP} = 0$ for small magnetic fields. Magnetic field's increasing leads to the growth of μ_{CEP} values and decrease in characteristic temperatures of the multivalued behavior, i.e. the temperatures of the background phase transition (corresponding to black hole – black hole collapse in AdS$_5$). Thus in the magnetic field strong enough background phase transition should occur at high chemical potentials and negligible temperatures.

3.2 Background phase transition

This is exactly the picture we observe on phase diagrams Fig. 5, obtained via free energy consideration

$$F = -\int s \, dT = \int_{z_h}^{\infty} s \, T' dz, \qquad (3.2)$$

where we normalize the free energy to vanish at $z_h \to \infty$. The background phase transition curves become shorter with the magnetic field increasing (larger c_B absolute values). Note, that two opposite tendencies can be seen: growth of the μ_{CEP} and decrease of the maximum chemical potential value. For $c_B \approx (-0.05; -0.03)$ depending on ν these
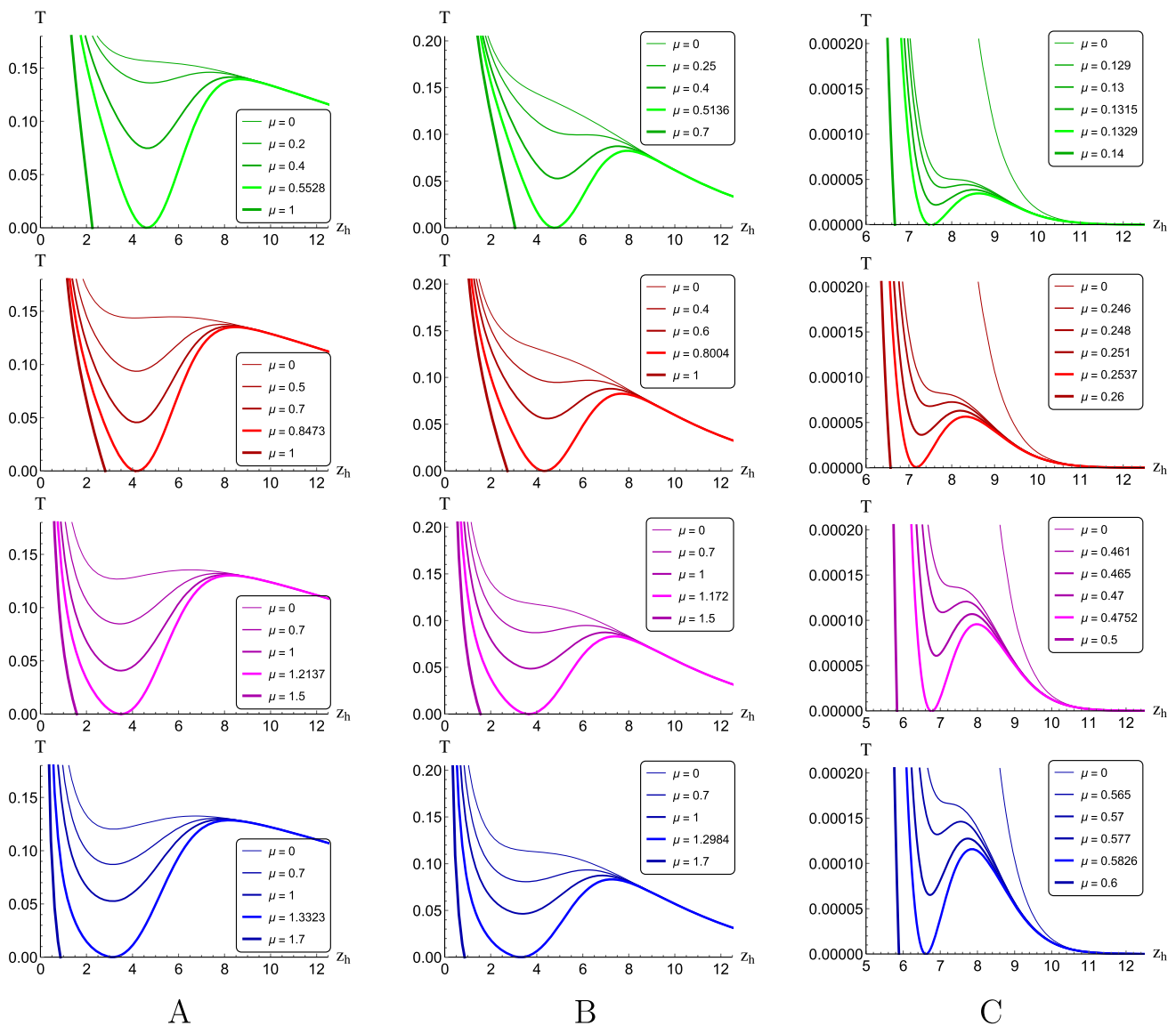
Fig. 4 Temperature as a function of horizon for different μ in isotropic (1-st line, green) and anisotropic cases for $\nu = 1.5$ (2-nd line, red), $\nu = 3$ (3-rd line, magenta), $\nu = 4.5$ (4-th line, blue) in magnetic field with $c_B = -0.001$ (**a**), $c_B = -0.01$ (**b**), $c_B = -0.1$ (**c**); $a = 4.046$, $b = 0.01613$, $c = 0.227$. Lighter curves show chemical potentials for which second horizon appears and multivalued behavior of $z_h(T)$-function actually turns into monotonian

tendencies come into conflict, and CEP curve reverses it's movement back towards lower values of the chemical potential (Fig. 6a).

Primary anisotropy affects the background phase transition for the light quarks QGP in much the same way as it did for the heavy quarks [9]: lowers transition temperatures and enlarges chemical potentials avaliable. But it almost doesn't influence the limit c_B values at which phase transition still exists. Phase transition temperatures reach negligible values at $c_B \approx -0.1$ almost regardless of primary anisotropy ν (Figs. 5a–d, 6b). It's effect on c_B for which μ_{CEP} becomes

non-zero is more notable: $c_B < -0.001$ for $\nu = 1.5$ and $\nu < -0.005$ for $\nu = 4.5$ (Fig. 6a, c).

We present CEP for $\nu = 1, 1.5, 3, 4.5$ in a three-dimensional space of parameters (μ, c_B, T) on Fig. 6d. Thus, figures A, B and C are the projections of a complete picture D on the corresponding planes. Also, one can see the smooth peach coloured surface of the first order phase transitions interpolating for intermediate values of anisotropy. The orange curve indicates boundaries of possible phase transition locations in this space of parameters.
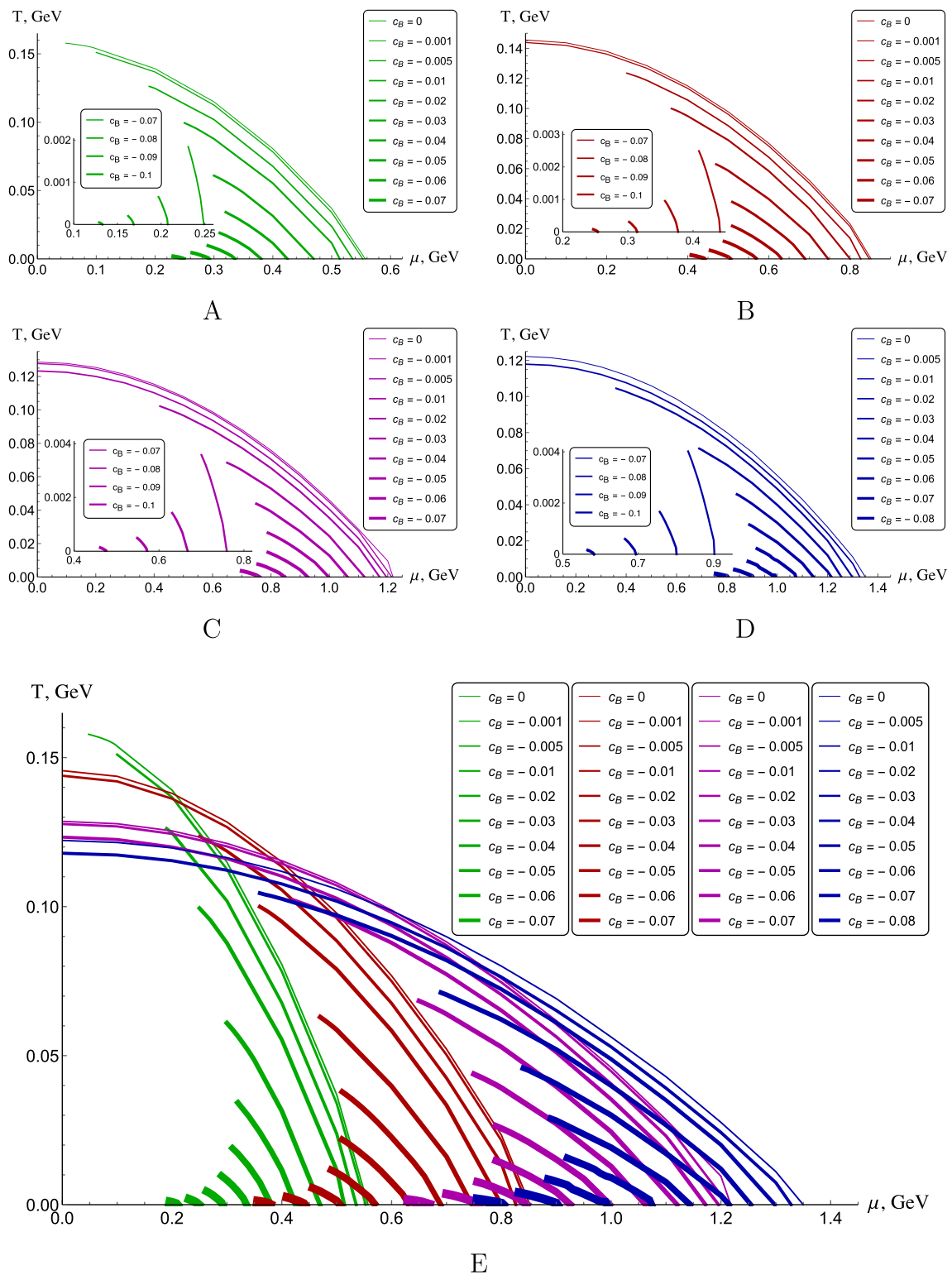
Fig. 5 Background phase transition diagram $T(\mu)$ in isotropic (**a**) and anisotropic cases for $\nu = 1.5$ (**b**), $\nu = 3$ (**c**), $\nu = 4.5$ (**d**) and all combined (**e**); $a = 4.046$, $b = 0.01613$, $c = 0.227$
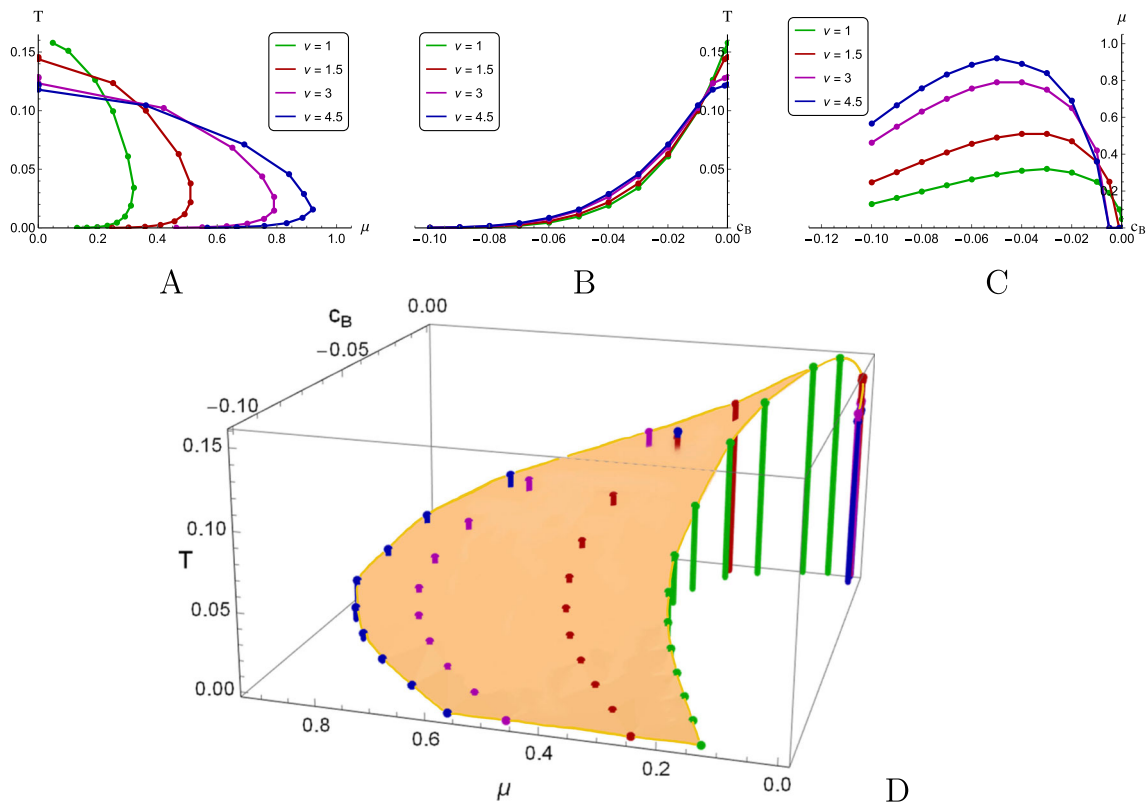
Fig. 6 CEP positions on the background phase transition diagram $T(\mu)$ in isotropic and anisotropic cases for $\nu = 1,\ 1.5,\ 3,\ 4.5$ on planes $\mu - T$ (**a**), $c_B - T$ (**b**), $c_B - \mu$ (**c**) and 3D plot $T(c_B, \mu)$ (**d**); $a = 4.046$, $b = 0.01613$, $c = 0.227$

3.3 Temporal Wilson loops

The expectation value of the temporal Wilson loop calculation does not differ from the heavy quarks case [9] untill we substitute the specific light quarks warp factor into the general expressions for the dynamical wall (DW) equations:

$$DW_x: \quad -\frac{4abz}{1+bz^2} + \sqrt{\frac{2}{3}}\phi'(z) + \frac{g'}{2g} - \frac{2}{z}\bigg|_{z=z_{DWx}} = 0,$$

$$DW_{y_1}: \quad -\frac{4abz}{1+bz^2}$$
$$+ \sqrt{\frac{2}{3}}\phi'(z) + \frac{g'}{2g} - \frac{\nu+1}{\nu z}\bigg|_{z=z_{DWy_1}} = 0, \quad (3.3)$$

$$DW_{y_2}: \quad -\frac{4abz}{1+bz^2}$$
$$+ \sqrt{\frac{2}{3}}\phi'(z) + \frac{g'}{2g} - \frac{\nu+1}{\nu z} + c_B z\bigg|_{z=z_{DWy_2}} = 0.$$

Primary anisotropy has significant influence on the Wilson loop transformations in the magnetic field (Fig. 7). For $\nu = 1$ the Wilson loop phase transition curve becomes less inclined and it's temperature decreases, while maximum chemical potential grows. At $c_B = -0.0000985$ the curve becomes

horizontal and for $c_B < -0.0000985$ it just disappears (Fig. 7a). For $\nu = 4.5$ larger absolute c_B also leads to lesser temperatures, but chemical potential decreases as well, so the Wilson loop curve shrinks clinging to the abscissa axis μ at the end. The curve disappears for $c_B < -0.0858$ (Fig. 7d). For intermediate values of primary anisotropy $\nu = 1.5$ (Fig. 7b) and $\nu = 3$ (Fig. 7c) a mixture of both these tendencies can be seen. But inverse magnetic catalysis takes place for any primary anisotropy.

Let us now consider the combination of the 1-st order phase transition and a crossover for the primary anisotropy and magnetic field fixed (while both transition curves do exist). On Fig. 8 regions of their intersection or approach are shown, and the general view of the phase diagrams can be found on the inserted mini-plots. Points of intersections, where the confinement/deconfinement main role passes from the crossover to the 1-st order phase transitions (or vice versa), are marked as (μ_{by_2}, T_{by_2}) (Table 1). Critical end points, where the 1-st order phase transition begins, are marked as CEP_{LQ}.

For the primary isotropic case $\nu = 1$ a crossover disappears very soon, so it's position relative to the 1-st order phase transition does not have time to change much. The intersection point just shifts to the larger μ and the lesser T.
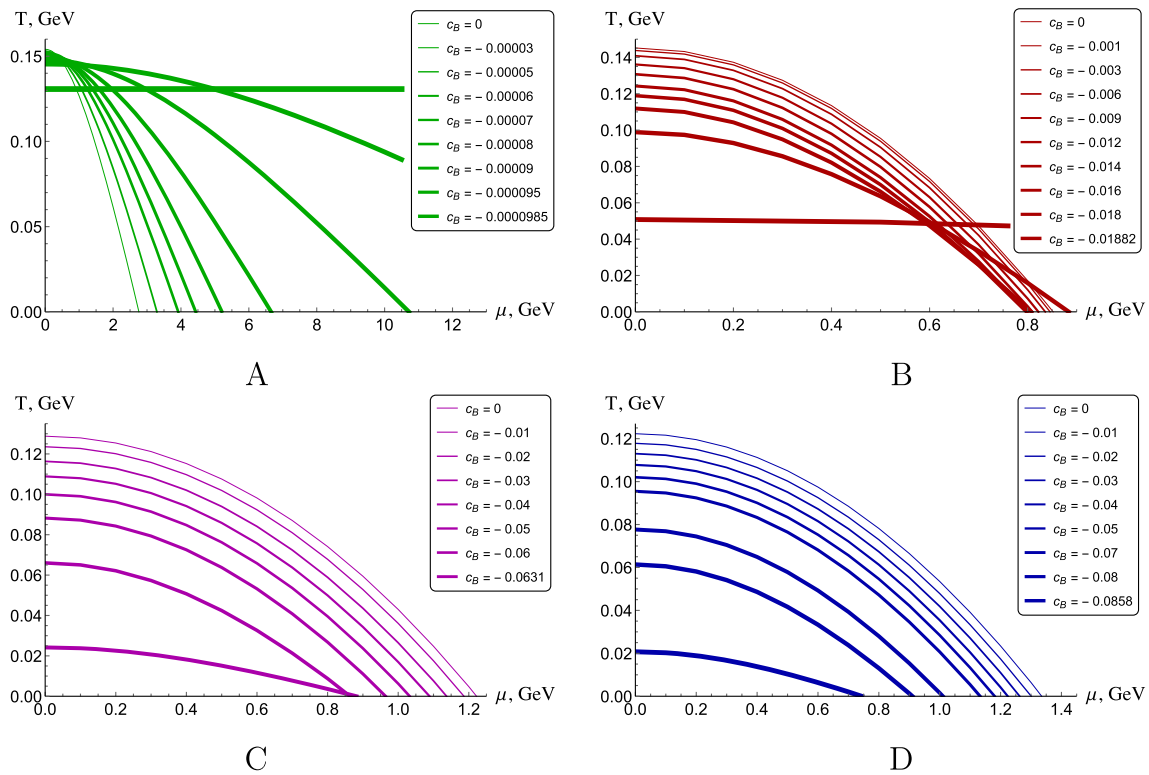
Fig. 7 Wilson loop phase transition curves $T(\mu)$ in isotropic (**a**) and anisotropic cases for $\nu = 1.5$ (**b**), $\nu = 3$ (**c**) and $\nu = 4.5$ (**d**); $a = 4.046$, $b = 0.01613$, $c = 0.227$

For $\nu = 1.5$ both curves are very close to each other and look cocentric. They do not intersect, so the crossover defines the phase transition for all chemical potential values. Magnetic field makes these curves closer to each other and hardly distinguishable, but the intersection appears at about $c_B = -0.018$ and coincides with the CEP_{LQ}. At this moment phase transition main role clearly passes from the crossover to the 1-st order phase transition though for rather a short interval. Before it's disappearance at $c_B = -0.01882$ the crossover line shifts down to lesser temperatures and becomes almost horizontal like it was for $\nu = 1$.

For $\nu = 3$ the 1-st order phase transition and a crossover can't be distiguished properly. Magnetic field shifts the 1-st order phase transition curve under the crossover, so that they do not intersect. Under these circumstances there is no smooth transfer between the crossover and the 1-st order phase transition, but a jump to lower temperature – temperature of CEP_{LQ}. Near the limit $c_B = -0.0631$ the crossover catches up with the 1-st order phase transition and a smooth transfer appears again just before the crossover vanishes.

For the maximal primary anisotropy $\nu = 4.5$ the 1-st order phase transition curve constantly shifts under the crossover curve, so that the intersection point moves to larger chemical potentials and lower temperatures. On the other hand CEP_{LQ} also moves, causing a jump transfer from the crossover to the 1-st order phase transition. The reverse transition is smooth.

For $c_B = -0.03$ the 1-st order phase transition is completely under the crossover so that the reverse transition does not occur, and further for $c_B < -0.03$ it occurs as a jump to higher temperatures. The 1-st order phase transition exists in a very narrow interval. So the confinement/deconfinement transition should be defined by a crossover with constantly decreasing temperature except a small local region of almost zero T. Near the limit value $c_B = -0.0858$ the crossover catches up with the 1-st order phase transition like it was for $\nu = 3$. Soon after this moment the crossover vanishes, but the 1-st order phase transition doesn't survive for long after that.

4 Electrical conductivity

Electrical conductivity contains information about transport and optical properties of a physical system. Understanding the behavior of the conductivity under different conditions is an essential step in studying properties of the direct photons.

4.1 Conductivity in anisotropic background

We use the model derived above to investigate properties of the direct photons formed in HIC. The detailed consideration of the holographic approach to electrical conductivity and
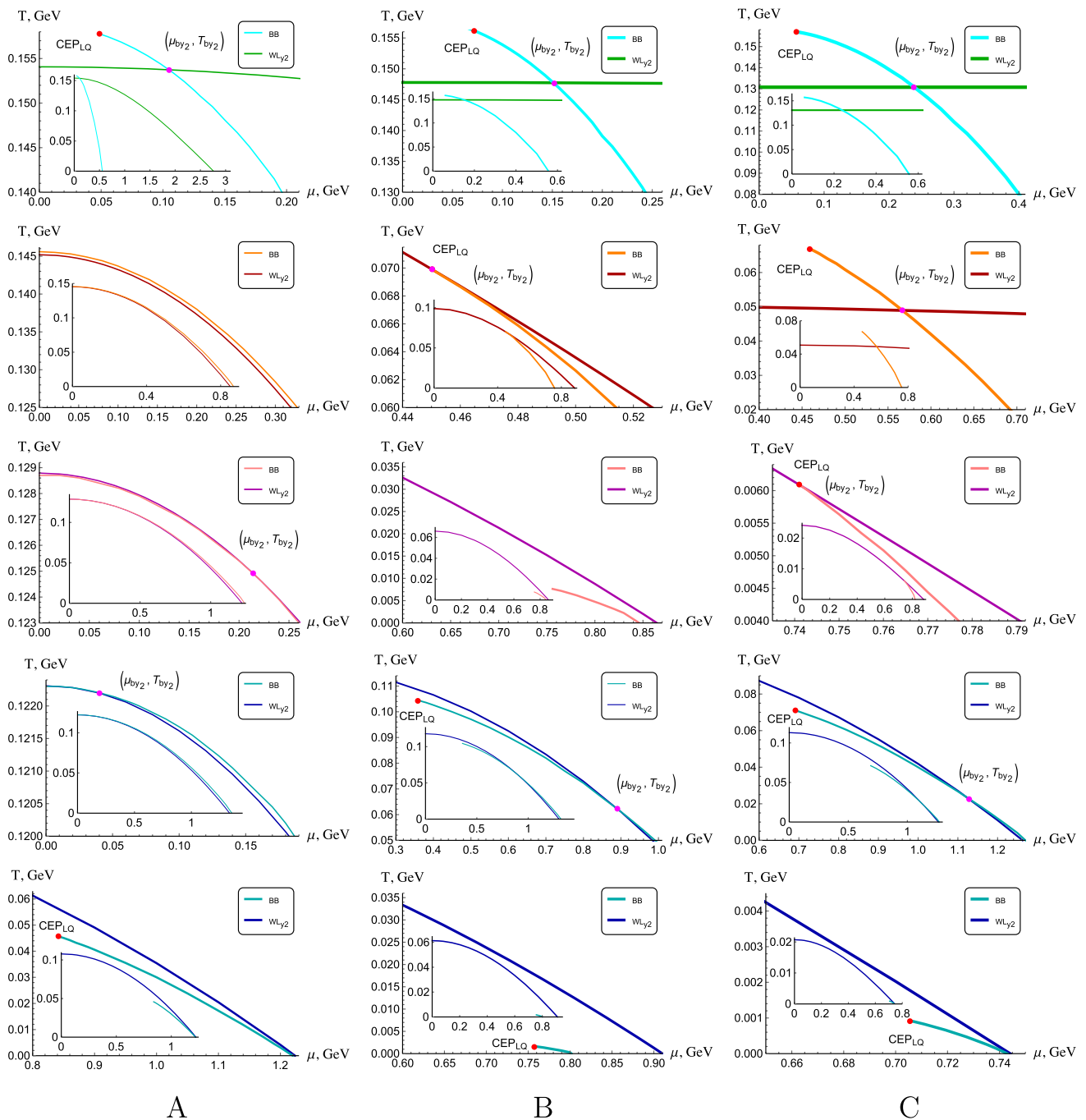
Fig. 8 Phase diagram (μ, T) as a combination of the 1-st order phase transition (BB) and a crossover (WL) in isotropic (1-st line, green) with $c_B = 0$ (**a**), $c_B = -0.00009$ (**b**), $c_B = -0.0000985$ (**c**), and anisotropic cases for $\nu = 1.5$ (2-nd line, red) with $c_B = 0$ (**a**), $c_B = -0.018$ (**b**), $c_B = -0.01882$ (**c**), $\nu = 3$ (3-rd line, magenta) with $c_B = 0$ (**a**), $c_B = -0.06$ (**b**), $c_B = -0.0631$ (**c**), $\nu = 4.5$ (4-th and 5-th line, blue), with $c_B = 0$ (**a**), $c_B = -0.01$ (**b**), $c_B = -0.02$, (**c**), $c_B = -0.03$ (**a**), $c_B = -0.08$ (**b**), $c_B = -0.0858$ (**c**); $a = 4.046$, $b = 0.01613$, $c = 0.227$

Table 1 Intersection points from the Wilson loop phase transition curve (crossover) to the background phase transition curve (1-st order phase transition) in $(\mu; T)$-coordinates depending on the primary anisotropy ν and the magnetic field's anisotropy c_B

	c_B	(μ_{by_2}, T_{by_2})
	0	(0.1049, 0.1531)
$\nu = 1$	-0.00009	(0.1405, 0.1479)
	-0.0000985	(0.2308, 0.1311)
	0	No intersection
$\nu = 1.5$	-0.018	(0.4501, 0.0699)
	-0.01882	(0.5622, 0.04928)
	0	(0.2148, 0.1249)
$\nu = 3$	-0.01	(0.9738, 0.03968), (1.124, 0.01188)
	$[-0.06, -0.02]$	No intersection
	-0.0631	(0.7409, 0.006101)
	0	(0.03893, 0.1222)
$\nu = 4.5$	-0.01	(0.8903, 0.06232)
	-0.02	(1.123, 0.02343)
	$[-0.0858, -0.03]$	No intersection

direct photon emission rate of QGP is presented in [32,49,62]. We briefly describe the framework for the holographic investigations of the electrical conductivity below.

In the anisotropic background[1]

$$
ds^2 = \frac{L^2 \mathfrak{b}(z)}{z^2}
$$
$$
\times \left[-g(z)dt^2 + \mathfrak{g}_1(z)dx_1^2 + \mathfrak{g}_2(z)dx_2^2 \right.
$$
$$
\left. + \mathfrak{g}_3(z)dx_3^2 + \frac{dz^2}{g(z)} \right] \tag{4.1}
$$

we consider a probe Maxwell field

$$
S_{pert} = -\frac{1}{4} \int d^5x \sqrt{-g} \, f_0(\phi) F_{MN} F^{MN}. \tag{4.2}
$$

We assume this creates no gravitational backreaction. Function $f_0(\phi)$ is called a gauge kinetic function and is used to fit the model with lattice data for the isotropic QGP at zero chemical potential and zero magnetic field [49].

Transport coefficients may be found within the linear response theory using the Kubo relations. Namely, the electrical conductivity is related to the retarded Green's functions of electric currents. Therefore, one is interested in a plane wave solution to (4.2), which will be holographically dual to $U(1)$ electric current J^μ of the boundary theory. We take the ansatz of a plane wave propagating along the x_3-direction. The wave

---

[1] Note that we get (2.3) from (4.1) after $x_1 \to x$, $x_2 \to y_1$ and $x_3 \to y_2$. We call x_1 the longitudinal direction, i.e. the direction along the collision axis, x_2 and x_3 the transversal directions, and $(x_1 x_2)$ are coordinates in a collision plane. The external magnetic field is aligned along x_3.

amplitude is a function of the "holographic coordinate" z only. The Green's function in a low frequency limit may be found either using the prescription by Iqbal and Liu [62] or Son and Starinets [63]. The equivalence of these approaches is demonstrated in [32]. The components of electric conductivity tensor are then

$$
\sigma^{11} = \frac{2f_0(z_h)}{z_h} \sqrt{\frac{b(z_h)\mathfrak{g}_3(z_h)\mathfrak{g}_2(z_h)}{\mathfrak{g}_1(z_h)}}, \tag{4.3}
$$

$$
\sigma^{22} = \frac{2f_0(z_h)}{z_h} \sqrt{\frac{b(z_h)\mathfrak{g}_3(z_h)\mathfrak{g}_1(z_h)}{\mathfrak{g}_2(z_h)}}, \tag{4.4}
$$

$$
\sigma^{33} = \frac{2f_0(z_h)}{z_h} \sqrt{\frac{b(z_h)\mathfrak{g}_1(z_h)\mathfrak{g}_2(z_h)}{\mathfrak{g}_3(z_h)}}, \tag{4.5}
$$

where z_h is the event horizon position [32].

4.2 Model tuning

To tune the model parameters we use the results of lattice calculations from [64]. These results are known for the isotropic QGP ($\nu = 1$) with a number of flavours $N_f = 3$ at zero chemical potential ($\mu = 0$) and without magnetic field ($c_B = 0$). Thus, we fit the behaviour of electrical conductivity to the lattice data in this simplest case using the gauge kinetic function $f_0(\phi)$. Then it is possible to calculate the conductivity in anisotropic case and for non-zero parameters. We take the gauge kinetic function in the following form

$$
f_0(\phi) = \frac{0.0023}{\mathrm{C}_{em}} \left[0.9 \exp\left(-\frac{\phi^2}{8.8}\right) + 0.11 \exp(-0.05\phi) \right], \tag{4.6}
$$

where $\mathrm{C}_{em} = 2e^2/3$ is electromagnetic constant for $N_f = 3$ and ϕ is the dilaton field.

Numerical calculation for the isotropic conductivity and the gauge function are shown on Fig. 9. Here the critical temperature is $T_c = 0.155$ GeV. It was calculated as a temperature of the BB phase transition for a given set of parameters. The conductivity increases with temperature growth and saturates some value close to the $\mathcal{N} = 4$ SYM plasma conductivity.

4.3 Isotropic case

The conductivity tensor in the isotropic ($\nu = 1$) case with zero magnetic field reduces to the single value $\sigma = \sigma^{ii}$ ($i = 1, 2, 3$), so the QGP provides equal resistance to direct photons in all directions. The dependence of the conductivity to the temperature ratio σ^{ii}/T on the temperature for different values of chemical potential is shown in Fig. 10a. The non-zero magnetic field kills the degeneracy between
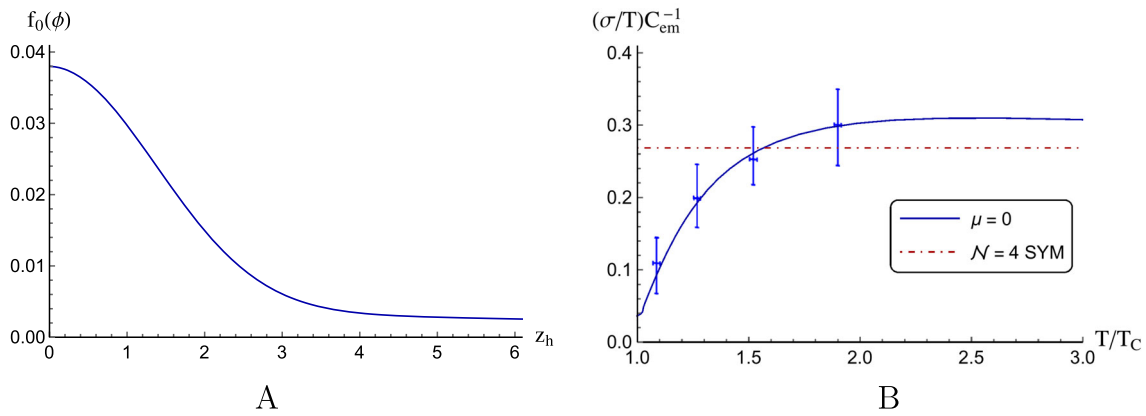
Fig. 9 Gauge kinetic function f_0 as a function of the horizon z_h (**a**) and relation of electrical conductivity to temperature σ/T as a function of the normalised temperature T/T_c (**b**): numerical calculations in our model for $\nu = 1$, $c_B = 0$ and $\mu = 0$ (the blue curve), lattice calculations from [64] (the blue dots with error bars) and the conductivity of $\mathcal{N} = 4$ SYM plasma (the red dash-dotted line)
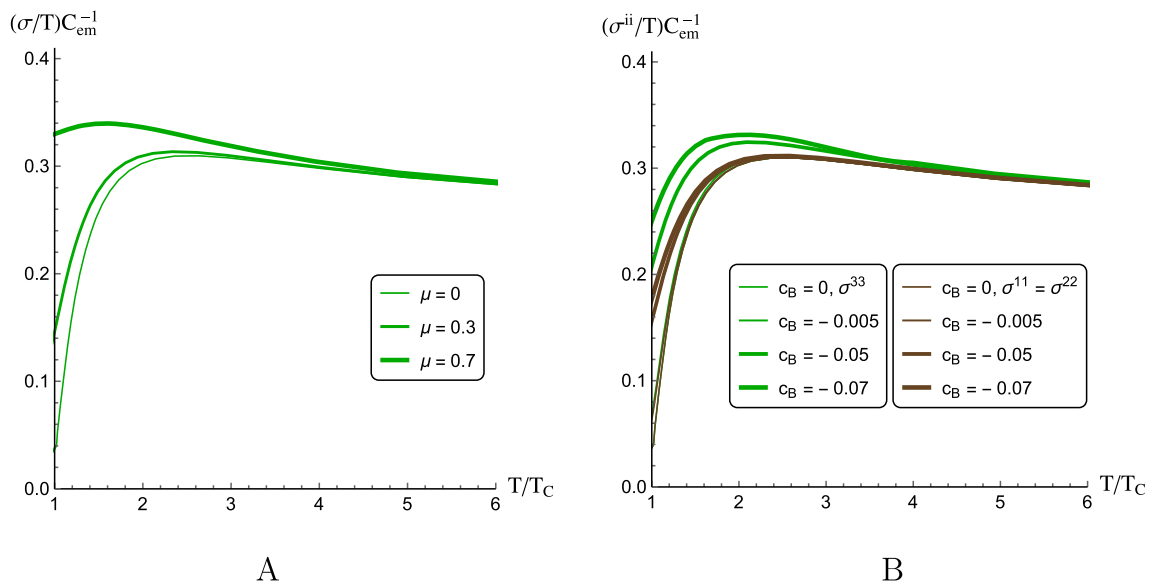

Fig. 10 The dependence of σ/T on the normalised temperature T/T_c in the isotropic case $\nu = 1$ for zero magnetic field $c_B = 0$ with different values of chemical potential $\mu = 0$, 0.3, 0.7 (**a**) and for zero chemical potential $\mu = 0$ with different values of the magnetic field parameter $c_B = 0$, -0.005, -0.05, -0.07 (magnetic field is directed along the x^3): σ^{33} (green curves) and $\sigma^{11} = \sigma^{22}$ (brown curves) (**b**)

two transverse directions (Fig. 10b). The plots presented in Fig. 10 demonstrate that the ratios σ^{ii}/T grow with the normalized temperature till some temperatures around $2T_c$. The precise location of the maximum depends on the chemical potential and the magnetic field values. At high temperatures the σ/T ratio decreases to some constant values near the conductivity of $\mathcal{N} = 4$ SYM plasma. Plots on Fig. 10a, b demonstrate the growth of conductivity with the magnetic field and/or chemical potential growing for the same temperature values. Also, one can see that in the directions orthogonal to the magnetic field the conductivity is lower than in a parallel one (brown curves are lower than the green ones of

the same thickness). Therefore, QGP is more opaque along the external magnetic fields.

4.4 Anisotropic case

In this subsection we study the electrical conductivity of QGP for the anisotropy parameter value $\nu = 4.5$. The results of numerical calculations of σ^{33}/T (conductivity along the external magnetic field) for different values of magnetic field and chemical potential are presented in Fig. 11.

We see that at the ratio σ^{33}/T decreases with temperature starting from $T = T_c$. The minimum position depends on the chemical potential and the external magnetic field value. The
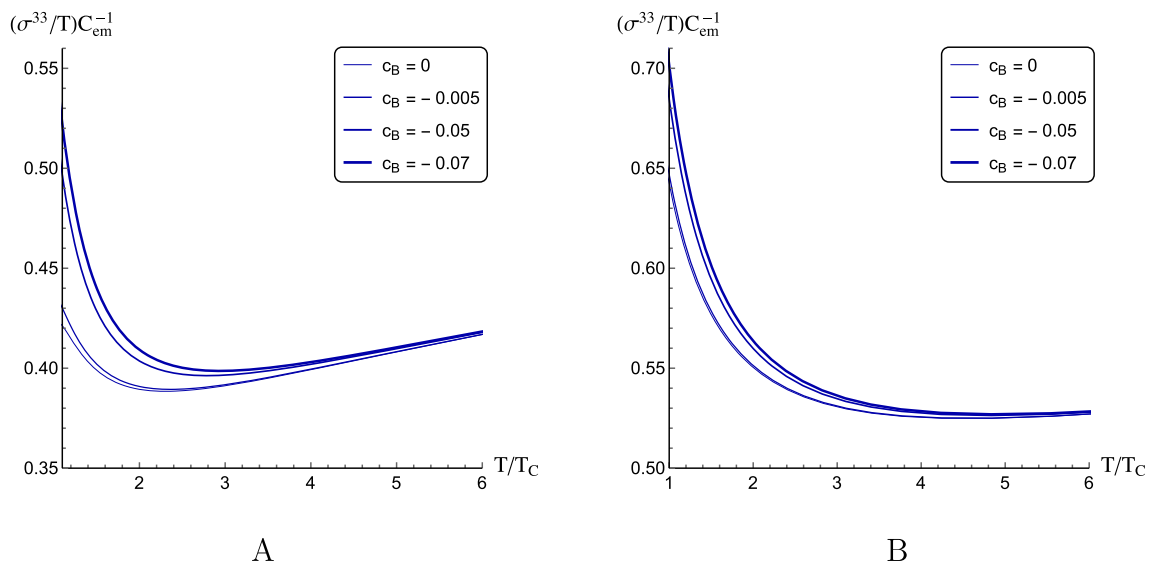
Fig. 11 The dependence of σ^{33}/T on the normalised temperature T/T_c in anisotropic case $\nu = 4.5$ for the magnetic field parameter $c_B = 0, -0.005, -0.05, -0.07$ with zero chemical potential $\mu = 0$ (**a**) and large chemical potential $\mu = 1$ (**b**); critical temperature $T_c = 0.121$ GeV

σ^{33}/T ratio after the minimum is greater for zero chemical potential and for lower magnetic fields. Stronger magnetic field and larger chemical potential increase the conductivity at the fixed temperature. One can see that at high temperatures the curves in Fig. 11 are getting closer to each other and almost coincide. Thus, anisotropic QGP with $\nu = 4.5$ along the external magnetic field direction is the most opaque at critical temperatures, becomes more transparent around $T \approx 2T_c$ for $\mu = 0$, Fig. 11a, and $T \approx 3.5T_c$ for $\mu = 1$, Fig. 11b, and after these values becomes more opaque with increasing temperature again.

Thermodynamic properties of σ^{22}/T are similar to those of σ^{33}/T and are shown in Fig. 12. We see that near the phase transition point σ^{22}/T decreases to a minimal value, and then starts to increase linearly at high temperatures. Plots in Fig. 12a, b show that higher the chemical potential is, higher the ratio σ^{22}/T becomes. However, the growth rate at high temperatures is larger for $\mu = 0$ case. The curves for strong and weak magnetic fields are almost indistinguishable, but the conductivity in stronger magnetic fields is greater than in weak ones. For zero magnetic field there is no difference between σ^{22} and σ^{33}, it can be seen in non-zero magnetic fields only. The value of σ^{33}/T is always larger than σ^{22}/T. The comparison of these two conductivity components can be found on Fig. 13.

The results of similar calculations for σ^{11}/T are shown in Fig. 14. We see that σ^{11}/T monotonically decreases to zero with temperature growth, while magnetic field and chemical potential push it down. Or, in other words, QGP along the collision line near the critical temperature is almost opaque and becomes transparent at high temperatures.

On Fig. 15 one can see the change of the conductivity behavior with the primary anisotropy parameter increasing. The green curves denote the isotropic case $\nu = 1$ and for the anisotropic cases the thicker line corresponds to the larger $\nu \neq 1$. As anisotropy increases, qualitative changes occur in all directions, where as usually two transverse and a longitudinal directions differ crucially. At low energies conductivity in longitudinal direction increases at low temperatures and starts decreasing after approximately $T = 2.5T_c$. At high values of anisotropy parameter ν longitudinal conductivity decreases monotonically. On the contrary, transverse components increase at high temperatures.

5 Conclusion

In this paper we have considered a twice anisotropic holographic model for the light quarks [12]. It is characterized by the Einstein-dilaton-three-Maxwell action and the five-dimensional metric with the warp factor that has been considered in isotropic case for the light quarks [7]. Our model has two different types of anisotropy mentioned above: the anisotropy related to the parameter ν (responsible for reproduction of the experimental energy dependence of multiplicity), and the anisotropy related to the external magnetic field (described by the third Maxwell field). The twice anisotropic model for the light quarks is much more complicated than the twice anisotropic model for heavy quarks [9,24], since the deformation factor and the kinetic gauge function f_1 have more compound form.

We have investigated the dependence of the phase transition structure on the anisotropy, characterized by parameter ν
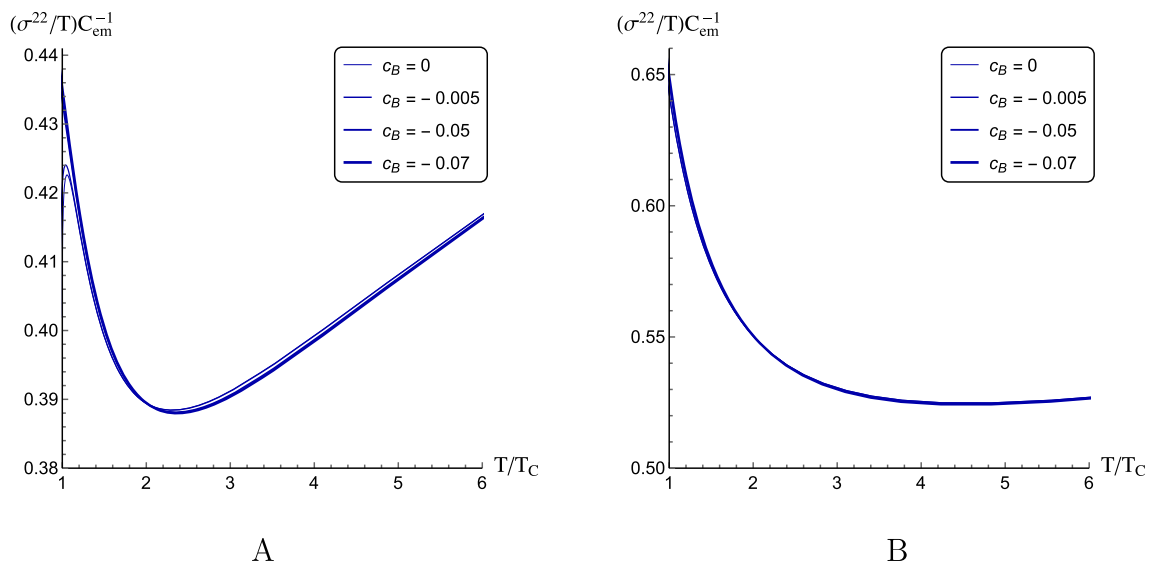
Fig. 12 The dependence of σ^{22}/T on the normalised temperature T/T_c in anisotropic case $\nu = 4.5$ for the magnetic field parameter $c_B = 0, -0.005, -0.05, -0.07$ with zero chemical potential $\mu = 0$ (**a**) and large chemical potential $\mu = 1$ (**b**); critical temperature $T_c = 0.121$ GeV
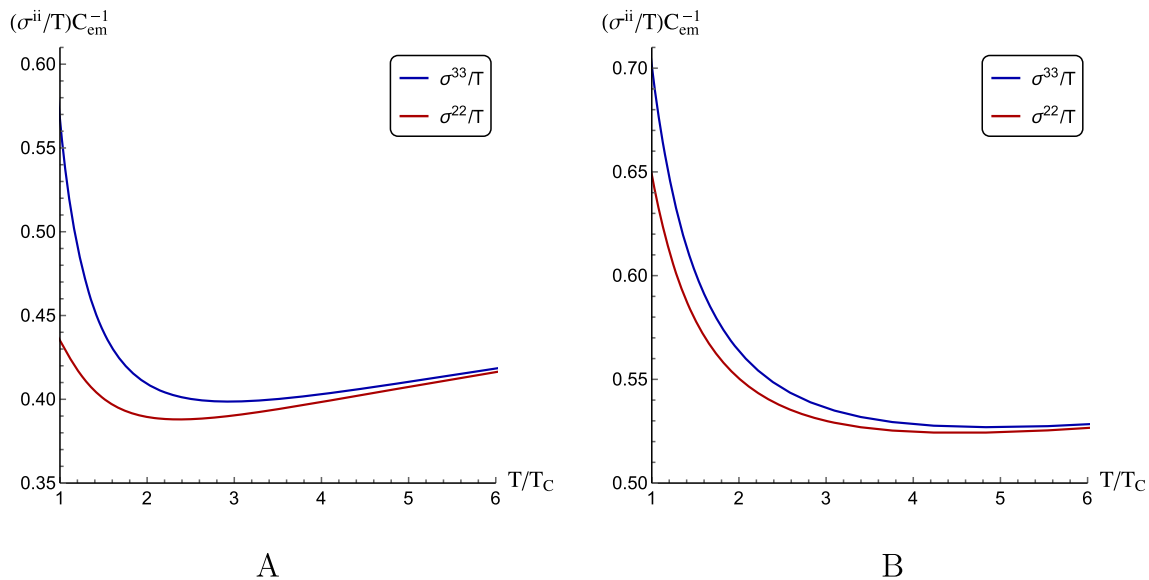

Fig. 13 The dependence of σ^{22}/T (red curves) and σ^{33}/T (blue curves) on the normalised temperature T/T_c in anisotropic case $\nu = 4.5$ for the magnetic field parameter $c_B = -0.07$ with zero chemical potential $\mu = 0$ (**a**) and large chemical potential $\mu = 1$ (**b**); critical temperature $T_c = 0.121$ GeV

and magnetic fields. The phase transition structure is set up by the mutual arrangement of two types of the phase transition lines – the 1-st order phase transition, originating from the metric background, and the crossover, originating from the temporal Wilson loop behavior. We have got the following results concerning the phase transition structure.

- For $\nu = 1$ the 1-st order phase transition in the light quarks model lasts from (μ_{CEP}, T_{CEP}) to $(\mu_{max}, 0)$. Magnetic field $c_B \neq 0$ shortens the 1-st order phase transition, increasing μ_{CEP} and decreasing μ_{max}. In the

heavy quarks model [9] the 1-st order phase transition lied from $(0, T_{max})$ to $(\mu_{CEP\,HQ}, T_{CEP\,HQ})$ almost horizontally. Magnetic field shortened this line just shifting $\mu_{CEP\,HQ}$ to zero. For the light quarks model the 1-st order phase transition line disappears at c_B about 7 times larger than it was for the heavy quarks model. Inverse magnetic catalysis is found for both models.

- For $\nu > 1$ primary anisotropy decreases temperature of the 1-st order phase transition and increases μ_{max}. It almost doesn't influence the c_B value that the 1-st order
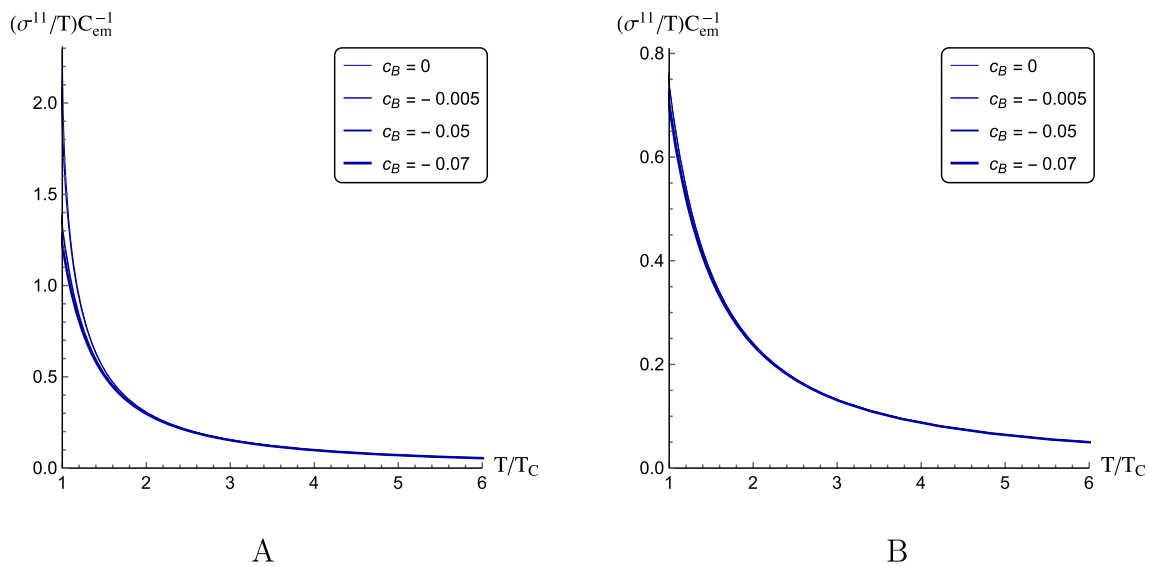
Fig. 14 The dependence of σ^{11}/T on the normalised temperature T/T_c in anisotropic case $\nu = 4.5$ for the magnetic field parameter $c_B = 0, -0.005, -0.05, -0.07$ with zero chemical potential $\mu = 0$ (**a**) and large chemical potential $\mu = 1$ (**b**); critical temperature $T_c = 0.121$ GeV

phase transition line disappears at, like it was for the heavy quarks model [9].

- For $\nu = 1$ magnetic field decreases the Wilson loop curve inclination until it becomes horizontal. This leads to the inverse magnetic catalysis effect for μ near zero and the direct magnetic catalysis for larger chemical potential values. In the heavy quarks model [9] the Wilson loop curve underwent the inverse magnetic catalysis only and shrinked tending to vertical T-axis.

- Primary anisotropy $\nu > 1$ decreases the Wilson loop phase transition temperature and the region of the direct magnetic catalysis. It also increases the absolute value of c_B at which the Wilson loop survives. For $\nu = 4.5$ the Wilson loop curve shrinks tending to horizontal μ-axis. For the heavy quarks model the larger anisotropy was the weaker it decreased the Wilson loop temperature.

- For $\nu = 1$ in the light quarks model the confinement/deconfinement phase transition is determined by the crossover from $\mu = 0$ to the intersection with the 1-st order phase transition μ_{by_2}, where it picks up the main role. On the opposite, for the heavy quarks model [9] the 1-st order phase transition was decisive from $\mu = 0$ to the intersection with the crossover μ_{by_2}.

- Magnetic field $c_B \neq 0$ for $\nu = 1$ shifts the intersection point (μ_{by_2}, T_{by_2}) to the larger chemical potentials and the lower temperatures, but doesn't actually change the general scheme for the light quarks model. For the heavy quarks model [9] the 1-st order phase transition moved to above the Wilson loop curve and lost it's influence on the confinement/deconfinement process.

- Anisotropy $\nu > 1$ makes the 1-st order phase transition to move under the Wilson loop curve. Therefore

the crossover determines the confinement/deconfinement process from $\mu = 0$ to μ_{CEP}, where the 1-st order phase transition begins and takes the main role with a jump. For the heavy quarks model [9] the 1-st order phase transition also moved under the Wilson loop curve and determined the confinement/deconfinement process from $\mu = 0$ to μ_{CEPHQ}, where the 1-st order phase transition ends and gives the main contribution to the crossover with a jump.

We have also studied the DC conductivity of the QGP in the deconfined phase under different conditions. The conductivity has different values and thermodynamic properties in the HIC direction and in the orthogonal plane presented, see Figs. 10 11, 12, 13 and 14.

- For $\nu = 1$ the conductivity
  - σ^{ii}/T near the critical temperature grows with the temperature up to $\approx 2T_c$ and then starts to decrease to a constant value near the conductivity of $\mathcal{N} = 4$ SYM plasma along all the directions;
  - along the orthogonal to the magnetic field directions is lower than in a parallel one;
  - grows with the chemical potential and the external magnetic field values.

- For $\nu = 4.5$ the conductivity
  - σ^{33}/T along the magnetic field direction has a minimum and increases at high temperatures (Fig. 11);
  - σ^{22}/T along the transversal direction also has a minimum followed by the increment at high temperatures (Fig. 12); σ^{33} and σ^{22} can be distinguished at the

Fig. 15 The dependence of σ^{11}/T (1-st line), σ^{22}/T (2-nd line) and σ^{33}/T (3-rd line) on the normalised temperature T/T_c for different ν with $\mu = 0$, $c_B = 0$ (**a**) and $\mu = 0.5$, $c_B = -0.05$ (**b**)
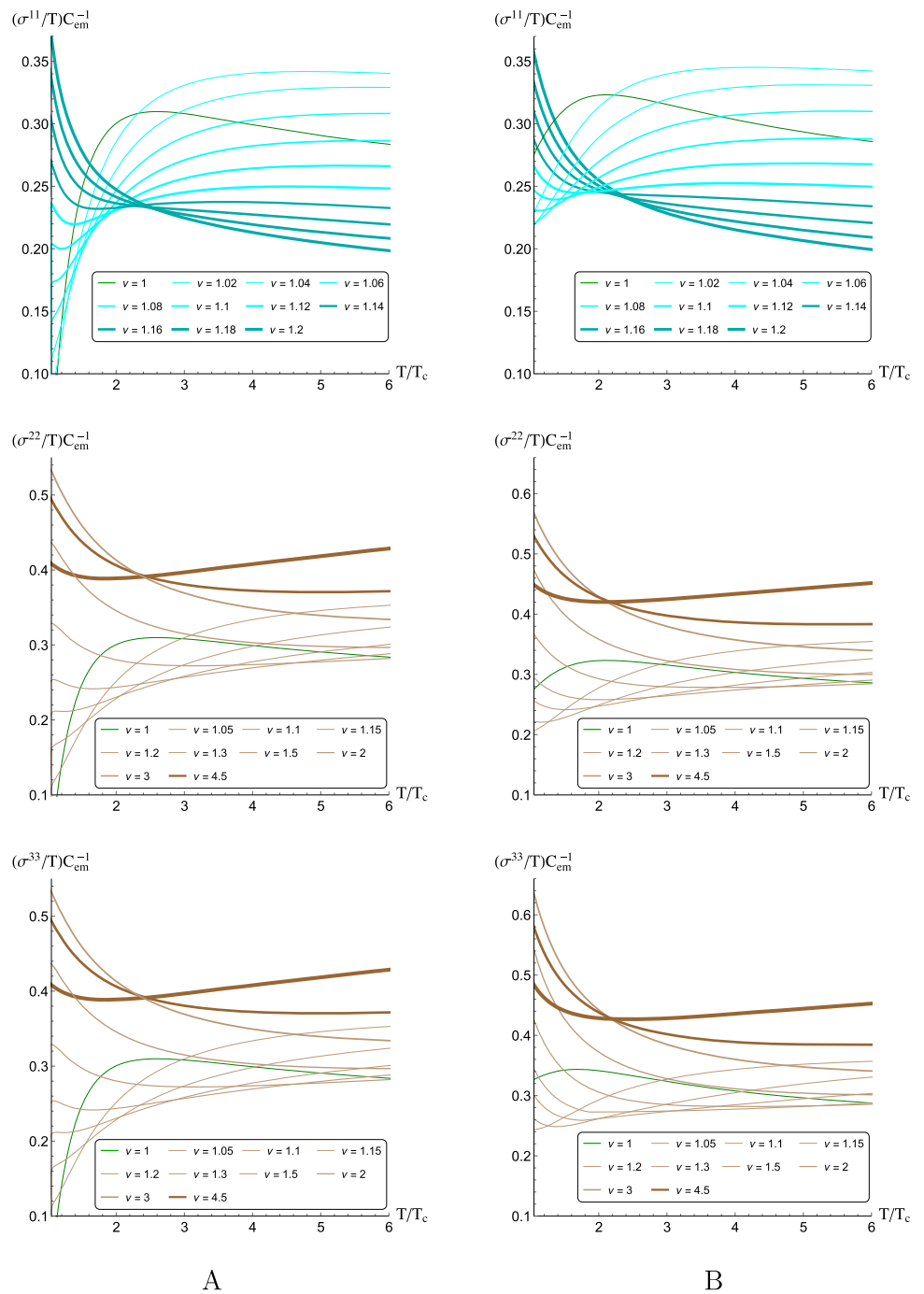
non-zero magnetic fields, and σ^{33} is always greater than σ^{22} (Fig. 13);

– σ^{11}/T along the longitudinal direction monotonically decreases (Fig. 14).

It is instructive to compare the conductivity for the light and heavy quarks. Let us remind that for the heavy quark model we had [32] the following picture.

- For $\nu = 1$

– at temperatures higher than the critical value the ratios σ^{ii}/T increase to the constant values depending on μ and c_B;

– increasing μ or magnetic field increases the values of these constant (saturation) values;

– the conductivity σ^{22} and σ^{33} are almost indistinguishable for small values of the external magnetic field.

- For $\nu = 4.5$ the conductivity

– σ^{22}/T and σ^{33}/T along the transversal directions increase with the temperature growth and saturate a certain value $\sigma^{22}/T \approx \sigma^{33}/T$ depending on the μ and magnetic field values;

– σ^{11}/T along the longitudinal direction approaches zero at high temperatures.

Thus, we see that for $\nu = 1$ the conductivity behavior for the heavy and light quarks is different at near-critical temperatures, but at high temperatures they saturate some constant values and these values increase with the chemical potential and magnetic field growth. The saturation constants are equivalent at zero μ and c_B. Isotropic QGP for the light quarks as well as for the heavy quarks is almost transparent in all directions near the critical temperature and become opaque at high temperature. The main difference between them may be seen at intermediate temperatures.

For $\nu = 4.5$ the conductivity behavior for the heavy and light quarks is different at near-critical temperature as well as for high temperatures. In particular, there is no saturation of σ^{33} and σ^{22} at high temperature for the light quarks, meanwhile these components of the conductivity for the heavy quarks reach a constant value at high temperature. The longitudinal component of the conductivity for the heavy quarks decreases to zero as it does for the light quarks.

There are some obvious open questions regarding our model that are worth exploring. Let us mention some of them. It would be interesting to study the quark potential for the light quark model considered here like it was done for the heavy quark model [65].

It would also be interesting to study the entanglement entropy (EE) behavior for our model. Note that EE was studied in the [15] model and was not studied either in the presence of an external magnetic field for the heavy quark model [9], or for the light quark model in the absence of an external magnetic field [11].

In the spirit of the jet quenching studying [66,67] for the simplest [15] model, it would be interesting to investigate the behavior of the jet quenching for the model considered in this article. Of particular interest is the consideration of the external magnetic field influence on the results.

In this paper we determine the MC/IMC as the increase/decrease of the first order phase transition temperature with increasing the magnetic field value. In lattice calculations the MC and IMC are determined as increase/decrease of the chiral phase transition temperature with increasing the value of magnetic field [68–71]. Note that the chiral phase transition coincides with the first order phase transition in the holographic model for heavy quarks [22], see also studies of the chiral condensate in holography in [72–76] and references therein. The study of the quark condensate and the chiral

phase transition is certainly of interest for the structure of the phase transitions for light quarks.

Data availability statement This manuscript has no associated data or the data will not be deposited. [Authors' comment: This is a theoretical study and no experimental data]

References

1. J. Casalderrey-Solana, H. Liu, D. Mateos, K. Rajagopal, U.A. Wiedemann, *Gauge/String Duality, Hot QCD and Heavy Ion Collisions* (Cambridge University Press, Cambridge, 2014). arXiv:1101.0618 [hep-th]
2. IYa. Aref'eva, Holographic approach to quark-gluon plasma in heavy ion collisions. Phys. Usp. **57**, 527 (2014)
3. O. DeWolfe, S.S. Gubser, C. Rosen, D. Teaney, Heavy ions and string theory. Prog. Part. Nucl. Phys. **75**, 86 (2014). arXiv:1304.7794 [hep-th]
4. U. Gursoy, E. Kiritsis, L. Mazzanti, F. Nitti, Holography and thermodynamics of 5D dilaton-gravity. JHEP **0905**, 033 (2009). arXiv:0812.0792 [hep-th]
5. U. Gursoy, E. Kiritsis, L. Mazzanti, G. Michalogiorgakis, F. Nitti, Improved holographic QCD. Lect. Notes Phys. **828**, 79–146 (2011). arXiv:1006.5461 [hep-th]
6. Y. Yang, P.H. Yuan, Confinement-deconfinement phase transition for heavy quarks in a soft wall holographic QCD model. JHEP **12**, 161 (2015). arXiv:1506.05930 [hep-th]
7. M.-W. Li, Y. Yang, P.-H. Yuan, Approaching confinement structure for light quarks in a holographic soft wall QCD model. Phys. Rev. D **96**, 066013 (2017). arXiv:1703.09184 [hep-th]
8. H.J. Pirner, B. Galow, Strong equivalence of the AdS-metric and the QCD running coupling. Phys. Lett. B **679**, 51–55 (2009). arXiv:0903.2701 [hep-ph]
9. I.Ya. Aref'eva, K. Rannu, P. Slepov, Holographic model for heavy quarks in anisotropic hot dense QGP with external magnetic field. JHEP **07**, 161 (2021). arXiv:2011.07023 [hep-th]
10. K. Rannu, I. Ya, P. Slepov. Aref'eva, Holographic model in anisotropic hot dense QGP with external magnetic field. Supl. Rev. Mex. Fis. **3**, 0308126 (2022)
11. I.Ya. Aref'eva, K. Rannu, P. Slepov, Holographic anisotropic model for light quarks with confinement-deconfinement phase transition. JHEP **06**, 090 (2021). arXiv:2009.05562 [hep-th]

12. I.Ya. Aref'eva, K.A. Rannu, P.S. Slepov, Anisotropic solution of the holographic model of light quarks with an external magnetic field. Theor. Math. Phys. **210**(3), 363–367 (2022)

13. I.Ya. Aref'eva, Holography for nonperturbative study of QFT. Phys. Part. Nucl. **51**(4), 489–496 (2020)

14. A. Ballon-Bayona, H. Boschi-Filho, E. FolcoCapossoli, D.M. Rodrigues, Criticality from EMD holography at finite temperature and density. Phys. Rev. D **102**(12), 126003 (2020). arXiv:2006.08810 [hep-th]

15. IYa. Aref'eva, K.A. Rannu, Holographic anisotropic background with confinement-deconfinement phase transition. JHEP **05**, 206 (2018). arXiv:1802.05652 [hep-th]

16. I.Ya. Aref'eva, K.A. Rannu, P.S. Slepov, Orientation dependence of confinement–deconfinement phase transition in anisotropic media. PLB **792**, 470 (2019). arXiv:1808.05596 [hep-th]

17. S. He, S.Y. Wu, Y. Yang, P.H. Yuan, Phase structure in a dynamical soft-wall holographic QCD model. JHEP **04**, 093 (2013). arXiv:1301.0385 [hep-th]

18. J. Chen, S. He, M. Huang, D. Li, Critical exponents of finite temperature chiral phase transition in soft-wall AdS/QCD models. JHEP **01**, 165 (2019). arXiv:1810.07019 [hep-ph]

19. I.Y. Aref'eva, Theoretical studies of the formation and properties of quark-gluon matter under conditions of high baryon densities attainable at the NICA experimental complex. Phys. Part. Nucl. **52**(4), 512–521 (2021)

20. P.S. Slepov, A way to improve the string tension dependence on temperature in holographic model. Phys. Part. Nucl. **52**(4), 560–563 (2021)

21. K.A. Rannu, Holographic model for light quarks in anisotropic background. Phys. Part. Nucl. **52**(4), 555–559 (2021)

22. M.W. Li, Y. Yang, P.H. Yuan, Analytic study on chiral phase transition in holographic QCD. JHEP **02**, 055 (2021). arXiv:2009.05694 [hep-th]

23. I.Y. Aref'eva, K.A. Rannu, P.S. Slepov, Spatial Wilson loops in a fully anisotropic model. Theor. Math. Phys. **206**(3), 400–409 (2021)

24. I.Y. Aref'eva, K. Rannu, P.S. Slepov, Anisotropic solutions for a holographic heavy-quark model with an external magnetic field. Theor. Math. Phys. **207**(1), 44–57 (2021)

25. U. Gürsoy, M. Järvinen, G. Nijs, J.F. Pedraza, On the interplay between magnetic field and anisotropy in holographic QCD. JHEP **03**, 180 (2021). arXiv:2011.09474 [hep-th]

26. I.Y. Aref'eva, K. Rannu, P. Slepov, Energy loss in holographic anisotropic model for heavy quarks in external magnetic field. arXiv:2012.05758 [hep-th]

27. J. Zhou, J. Ping, Holographic Schwinger effect in anisotropic media. arXiv:2101.08105 [hep-th]

28. D. Dudal, A. Hajilou, S. Mahapatra, A quenched 2-flavour Einstein–Maxwell-dilaton gauge-gravity model. Eur. Phys. J. A **57**(4), 142 (2021). arXiv:2103.01185 [hep-th]

29. N.G. Caldeira, E. Folco Capossoli, C.A.D. Zarro, H. Boschi-Filho, Fluctuation and dissipation within a deformed holographic model at finite temperature and chemical potential. arXiv:2104.08397 [hep-th]

30. X. Chen, L. Zhang, D. Hou, Running coupling constant at finite chemical potential and magnetic field from holography. arXiv:2108.03840 [hep-ph]

31. M. Ali-Akbari, M. Lezgi, Note on stability and holographic subregion complexity. Eur. Phys. J. C **82**(2), 114 (2022). arXiv:2110.05793 [hep-th]

32. I.Y. Aref'eva, A. Ermakov, P. Slepov, Direct photons emission rate and electric conductivity in twice anisotropic QGP holographic model with first-order phase transition. Eur. Phys. J. C **82**(1), 85 (2022). arXiv:2104.14582 [hep-th]

33. O. Andreev, V.I. Zakharov, On heavy-quark free energies, entropies, Polyakov loop, and AdS/QCD. JHEP **04**, 100 (2007). arXiv:0611304 [hep-ph]

34. F.R. Brown, F.P. Butler, H. Chen, N.H. Christ, Zh. Dong, W. Schaffer, L.I. Unger, A. Vaccarino, On the existence of a phase transition for QCD with three light quarks. Phys. Rev. Lett. **65**, 2491–2494 (1990)

35. O. Philipsen, C. Pinke, The $N_f = 2$ QCD chiral phase transition with Wilson fermions at zero and imaginary chemical potential. Phys. Rev. D **93**(11), 114507 (2016). arXiv:1602.06129 [hep-lat]

36. J. Adam et al. [ALICE Collaboration], Centrality dependence of the charged-particle multiplicity density at midrapidity in Pb-Pb collisions at $\sqrt{s_{NN}} = 5.02$ TeV. Phys. Rev. Lett. **116**(22), 222302 (2016). arXiv:1512.06104 [nucl-ex]

37. I.Y. Aref'eva, A.A. Golubtsova, Shock waves in Lifshitz-like spacetimes. JHEP **04**, 011 (2015). arXiv:1410.4595 [hep-th]

38. V. Toneev, O. Rogachevsky, V. Voronyuk, Evidence for creation of strong electromagnetic fields in relativistic heavy-ion collisions. Eur. Phys. J. A **52**(8), 264 (2016). arXiv:1604.06231 [hep-ph]

39. R. Rougemont, R. Critelli, J. Noronha, Holographic calculation of the QCD crossover temperature in a magnetic field. Phys. Rev. D **93**, 045013 (2015). arXiv:1505.07894 [hep-ph]

40. D. Li, M. Huang, Y. Yang, P.H. Yuan, Inverse magnetic catalysis in the soft-wall model of AdS/QCD. JHEP **02**, 030 (2017). arXiv:1610.04618 [hep-th]

41. U. Gursoy, I. Iatrakis, M. Jarvinen, G. Nijs, Inverse magnetic catalysis from improved holographic QCD in the Veneziano limit. JHEP **03**, 053 (2017). arXiv:1611.06339 [hep-th]

42. D. Dudal, S. Mahapatra, Confining gauge theories and holographic entanglement entropy with a magnetic field. JHEP **04**, 031 (2017). arXiv:1612.06248 [hep-th]

43. U. Gursoy, M. Jarvinen, G. Nijs, Holographic QCD in the Veneziano limit at finite magnetic field and chemical potential. Phys. Rev. Lett. **120**, 242002 (2018). arXiv:1707.00872 [hep-th]

44. U. Gursoy, M. Jarvinen, G. Nijs, J.F. Pedraza, Inverse anisotropic catalysis in holographic QCD. Phys. Rev. Lett. **04**, 071 (2019). arXiv:1811.11724 [hep-th]

45. H. Bohra, D. Dudal, A. Hajilou, S. Mahapatra, Anisotropic string tensions and inversely magnetic catalyzed deconfinement from a dynamical AdS/QCD model. Phys. Lett. B **801**, 135184 (2020). arXiv:1907.01852 [hep-th]

46. S. He, Y. Yang, P.H. Yuan, Analytic study of magnetic catalysis in holographic QCD. arXiv:2004.01965 [hep-th]

47. D.M. Rodrigues, D. Li, E. Folco Capossoli, H. Boschi-Filho, Finite density effects on chiral symmetry breaking in a magnetic field in 2 + 1 dimensions from holography. Phys. Rev. D **103**, 6 (2021). arXiv:2010.06762 [hep-th]

48. I.Y. Aref'eva, A. Patrushev, P. Slepov, Holographic entanglement entropy in anisotropic background with confinement–deconfinement phase transition. JHEP **07**, 043 (2020). arXiv:2003.05847 [hep-th]

49. I. Iatrakis, E. Kiritsis, C. Shen, D. Yang, Holographic photon production in heavy ion collisions. JHEP **04**, 035 (2017). arXiv:1609.07208 [hep-ph]

50. S.Y. Wu, D.L. Yang, Holographic photon production with magnetic field in anisotropic plasmas. JHEP **08**, 032 (2013). arXiv:1305.5509 [hep-th]

51. S.I. Finazzo, J. Noronha, Holographic calculation of the electric conductivity of the strongly coupled quark-gluon plasma near the deconfinement transition. Phys. Rev. D **89**(10), 106008 (2014). arXiv:1311.6675 [hep-th]

52. G. Arciniega, F. Nettel, P. Ortega, L. Patiño, Brighter Branes, enhancement of photon production by strong magnetic fields in the gauge/gravity correspondence. JHEP **04**, 192 (2014). arXiv:1307.1153 [hep-th]

53. I. Aref'eva, Holography for heavy ions collisions at LHC and NICA. EPJ Web Conf. **164**, 01014 (2017). arXiv:1612.08928 [hep-th]
54. D. Ávila, T. Monroy, F. Nettel, L. Patiño, "Emission of linearly polarized photons in a QGP from the gauge/gravity correspondence", arXiv:2101.08802 [hep-th]
55. S. Caron-Huot, P. Kovtun, G.D. Moore, A. Starinets, L.G. Yaffe, Photon and dilepton production in supersymmetric Yang–Mills plasma. JHEP **12**, 015 (2006). arXiv:0607237 [hep-th]
56. L. Patino, D. Trancanelli, Thermal photon production in a strongly coupled anisotropic plasma. JHEP **02**, 154 (2013). arXiv:1211.2199 [hep-th]
57. M. Ammon, J. Erdmenger, *Gauge/Gravity Duality: Foundations and Applications* (Cambridge University Press, Cambridge, 2015)
58. J.I. Kapusta, C. Gale, in *Finite-Temperature Field Theory: Principles and Applications, Cambridge Monographs on Mathematical Physics*
59. D. Giataganas, Probing strongly coupled anisotropic plasma. JHEP **07**, 031 (2012). arXiv:1202.4436 [hep-th]
60. M. Strickland, Thermalization and isotropization in heavy-ion collisions. Pramana **84**, 671 (2015)
61. E. D'Hoker, P. Kraus, Charged magnetic brane solutions in AdS (5) and the fate of the third law of thermodynamics. JHEP **03**, 095 (2010). arXiv:0911.4518 [hep-th]
62. N. Iqbal, H. Liu, Universality of the hydrodynamic limit in AdS/CFT and the membrane paradigm. Phys. Rev. D **79**, 025023 (2009). arXiv:0809.3808 [hep-th]
63. D.T. Son, A.O. Starinets, Minkowski space correlators in AdS/CFT correspondence: recipe and applications. JHEP **09**, 042 (2002). arXiv:0205051 [hep-th]
64. G. Aarts, C. Allton, A. Amato, P. Giudice, S. Hands, J.I. Skullerud, Electrical conductivity and charge diffusion in thermal QCD from the lattice. JHEP **02**, 186 (2015). arXiv:1412.6411 [hep-lat]
65. I. Aref'eva, K. Rannu, P. Slepov, Cornell potential for anisotropic QGP with non-zero chemical potential. EPJ Web Conf. **222**, 03023 (2019)
66. D.S. Ageev, I.Y. Aref'eva, A. Golubtsova, Holographic Wilson loops in spacetimes with spatial anisotropy. PoS **CORFU2016**, 086 (2017)
67. D.S. Ageev, I.Y. Aref'eva, A.A. Golubtsova, E. Gourgoulhon, Thermalization of holographic Wilson loops in spacetimes with spatial anisotropy. Nucl. Phys. B **931**, 506–536 (2018). arXiv:1606.03995 [hep-th]
68. K. Fukushima, Y. Hidaka, Magnetic catalysis versus magnetic inhibition. Phys. Rev. Lett. **110**(3), 031601 (2013). arXiv:1209.1319 [hep-ph]
69. J.O. Andersen, W.R. Naylor, A. Tranberg, Phase diagram of QCD in a magnetic field: a review. Rev. Mod. Phys. **88**, 025001 (2016). arXiv:1411.7176 [hep-ph]
70. K.A. Mamo, Inverse magnetic catalysis in holographic models of QCD. JHEP **05**, 121 (2015). arXiv:1501.03262 [hep-th]
71. V.A. Miransky, I.A. Shovkovy, Quantum field theory in a magnetic field: from quantum chromodynamics to graphene and Dirac semimetals. Phys. Rep. **576**, 1–209 (2015). arXiv:1503.00732 [hep-ph]
72. D. Li, M. Huang, Chiral phase transition of QCD with $N_f = 2+1$ flavors from holography. JHEP **02**, 042 (2017). arXiv:1610.09814 [hep-ph]
73. Z. Fang, L. Zhang, Chiral transition and meson melting with finite chemical potential in an improved soft-wall AdS/QCD model. arXiv:1910.02269 [hep-ph]
74. A. Ballon-Bayona, L.A.H. Mamani, Nonlinear realization of chiral symmetry breaking in holographic soft wall models. Phys. Rev. D **102**(2), 026013 (2020). arXiv:2002.00075 [hep-ph]
75. P. Colangelo, F. De Fazio, N. Losacco, Chaos in a $Q\bar{Q}$ system at finite temperature and baryon density. Phys. Rev. D **102**, 074016 (2020). arXiv:2007.06980 [hep-ph]
76. H. Bohra, D. Dudal, A. Hajilou, S. Mahapatra, Chiral transition in the probe approximation from an Einstein–Maxwell-dilaton gravity model. Phys. Rev. D **103**, 8 (2021). arXiv:2010.04578 [hep-th]